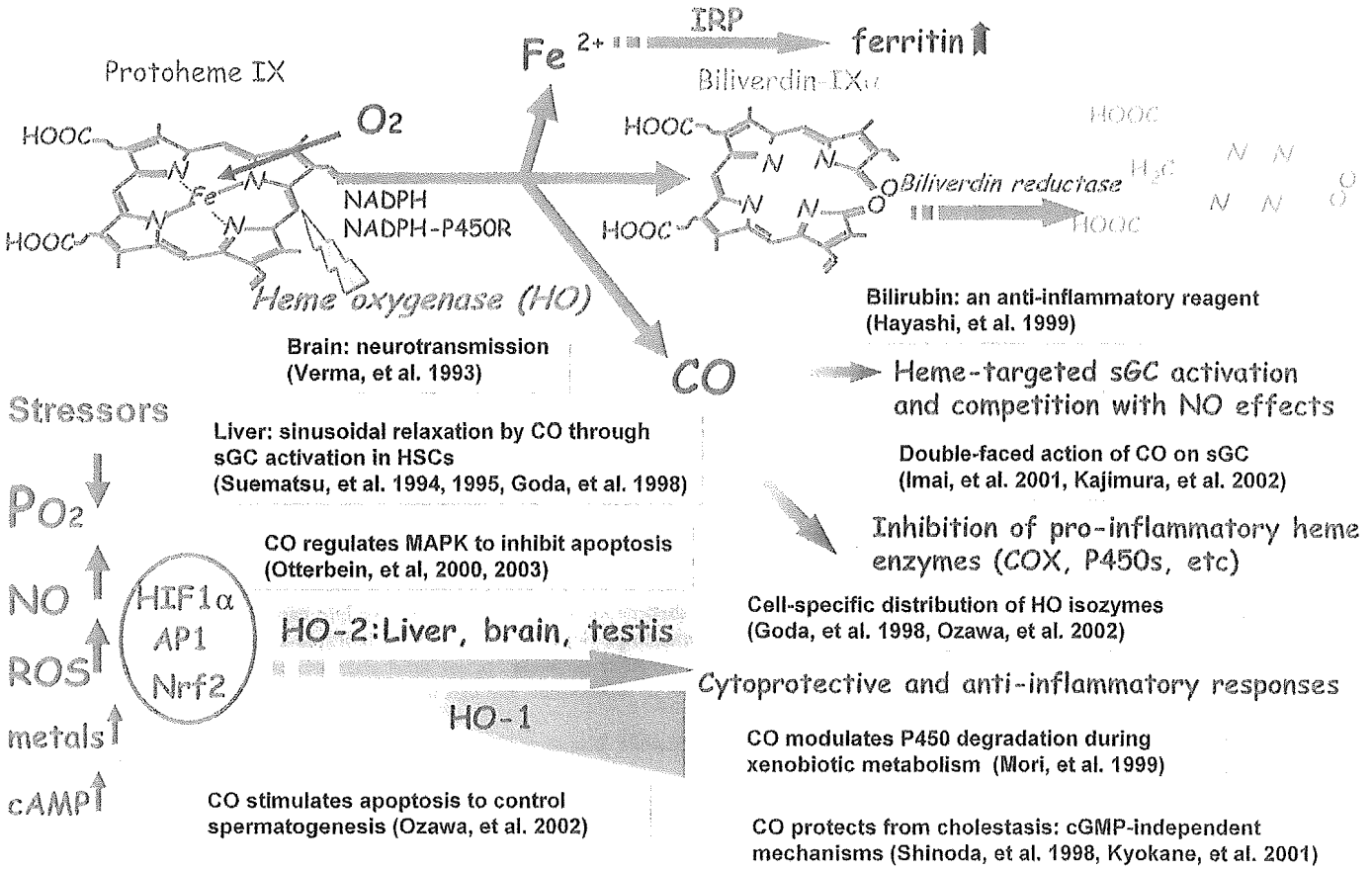

Fig. 1. Multiple mechanisms for organ homeostasis through the action of the heme oxygenase-CO system. sGC, soluble guanylate cyclase; COX, cyclooxygenase; IRP, iron responsive protein. Numbers in parenthesis indicate those in the reference list.

hemoglobin-derived heme and biliary excretion of bilirubin-IXα, a product generated from biliverdin-IXα through biliverdin reductase. In the rat perfused liver, approximately 0.5–0.7 μmol/min/g liver of CO is detectable, and stoichiometrically comparable amounts of glucuronyl bilirubin-IXα are excreted into bile (Yamaguchi et al., 1996; Suematsu and Ishimura, 2000). We demonstrated intrahepatic distribution of two major HO isozymes immunohistochemically, with the finding that the two isozymes have distinct topographic patterns; HO-1, the inducible form, is expressed prominently in Kupffer cells, while the constitutive HO-2 is abundant in hepatocytes (Goda et al., 1998). CO derived from HO-2 is necessary to keep sinusoids in a relaxing state through mechanisms involving sGC in hepatic stellate cells (HSC), also known as Ito cells that constitute microvascular pericytes in this organ. HSC cultured on silicon membrane-coated dishes exhibited wrinking formation through their intercellular connection of cytoplasmic processes and can respond to micromolar levels of CO to reduce the density of wrinkles; this event occurs in parallel with an elevation of cyclic GMP (Goda et al., 1998; Suematsu and Ishimura, 2000). Considering the microanatomical orientation of the liver cells in and around sinusoids, HO-2 in parenchyma stands in the reasonable position for the gas reception by HSC where CO released from hepatocytes can directly access to the cells and thereby modulate their contractility without being captured by hemoglobin in circulation.

When exposed to disease conditions such as advanced cirrhosis, the human liver upregulates HO-1 in Kupffer cells and hepatocytes as a result of cytokine responses (Makino et al., 2001). Under these circumstances, NOS activities seem to be downregulated. In experimental models of endotoxemia, such an induction of HO-1 is preceded by overproduction of NO derived from inducible NOS2 (Shiomi et al., 1998; Kyokane et al., 2001). Excess NO could cause the HO-1 induction and result in downregulation of NO, forming a feedback mechanism, through multiple mechanisms involving competition of NADPH as an electron donor for NOS and HO, degradation of the prosthetic heme for NOS, and inhibition of NOS by CO through its binding to the prosthetic heme group of the enzyme (Suematsu and Ishimura, 2000). The HO-1 induction expands the ability of liver to degrade heme and to trigger overproduction of CO (Wakabayashi et al., 1997; Kyokane et al. 2001). As discussed in the following section and also depicted in Fig. 1, CO turned out to contribute to maintenance of blood perfusion as well as that of bile excretion. Note that protective effects of HO against the liver dysfuction are not only attributable to those of CO but also to

actions of bilirubin, a potent anti-inflammatory and antioxidative compound generated by the same enzyme system (Hayashi et al. 1999; Kato et al. 2003).

HEPATIC DETOXIFICATION PROCESSES AND THE HO-CO SYSTEM

Elimination of constitutive CO by zinc protoporphyrin-IX, an HO inhibitor, not only increases sinusoidal tone but also stimulates bile acid-dependent bile flow (Sano et al., 1997). The choleretic response elicited by the HO inhibitor is reproduced by administration of oxyhemoglobin which captures both CO and NO, but not by methemoglobin which captures only NO, suggesting involvement of CO in modulation of bile acid-dependent bile flow (Kyokane et al. 2001). On the other hand, stress-inducible levels of CO cause choleresis through different mechanisms: in the perfused rat liver, CO up to 4-5 μmol/liter dose-dependently stimulates bile output concurrently with increases in bilirubin-IXα and glutathione in bile, though further elevation of the gas causes a reduction of the output. Under these circumstances, bile acid transport is reduced by contrast. Since Eizai hyperbilirubimenia rats do not exhibit such a choleretic response to CO, mechanisms appear to involve mrp2 (Norimizu et al., 2003). Although the detailed mechanisms have not fully been investigated, such a choleretic effect of CO helps detoxification processes under stress conditions, and might contribute to maintain the basal bile output driven through bile salt-independent fraction of the bile (Boyer and Klatskin, 1970).

Another important component responsible for CO-mediated regulation of biliary function is bile canaliculus which are composed of plasma membrane of adjacent hepatocytes. CO generated in hepatocytes may affect bile excretion through altering the contractility of bile canaliculi (BC) (Shinoda et al., 1998). According to analyses in rat hepatocytes couplets using time-lapse videomicroscopy, BCs contract with a periodicity of approximately 6-7 min. When consititutive CO is eliminated by the HO inhibitor, the intervals shorten and stroke volumes decrease in parallel with an increase in intracellular Ca^{2+}, suggesting that optimal concentrations of CO are necessary to maintain effective BC contraction. Addition of CO at a micromolar level reverses these changes without increasing cGMP, unlike the choleretic effect of NO (Trauner et al., 1997). Mechanisms of such a CO effect appear to involve modulation of cytochrome P-450-derived metabolites that are responsible for intracellular Ca^{2+} mobilization or modulation of potassium channels.

Upon excess administration of xenobiotics such as acetaminophen which is degraded via cytochrome P-450 monooxygenases, the liver overproduces CO at least through two distinct mechanisms: this event results from degradation of cytochrome P-450 by active intermediates such as NAPQI that secondarily increase heme available for HO-2 in hepatocytes (Mori et al., 1999). Later after the onset of centrilobular necrosis, HO-1 is induced in the liver that could further increase CO. In the acetaminophen-induced liver injury model, CO elicits an increase in paracellular junctional permeability and a decrease in transcellular vesicular transport. Under these circumstances, CO could act as a cholestatic factor. However, its protective properties could also be envisoned if opening of the paracellular pathway allows excretion of reactive toxic intermediates and the increase in CO slows the cytochrome P-450–mediated generation of toxic compounds.

CO- AND NO-MEDIATED SIGNAL TRANSDUCTION: ANALOGY OR DIFFERENCE?

How can our biological systems distinguish CO and NO as signal transducing triggers? We can learn fundamental differences in biochemical properties of the gases through structural behavior of hemoglobin after each gas is bound to the prosthetic heme of the protein (Fig. 2). CO stabilizes the six-coordinated form of the prosthetic heme and increases the affinity of molecular oxygen in other subunits (R-state), whereas NO binds to the α subunit of the heme and breaks the proximal histidine-Fe bond, forming a five-coordinated nitrosyl heme complex to decrease the affinity of oxygen in β subunits (T-state) (Yonetani et al., 1998; Suganuma et al., in press). Such an effect of NO for the T-state stabilization makes human erythrocytes a possible therapeutic tool for treating ischemic liver damages: despite halved oxygen-carrying capacity, αNO-erythrocytes deliver comparable amounts of oxygen to the ischemic liver tissue and stimulates oxygen consumption to improve bile output (Suganuma et al., 2005). This is partly because the binding of NO to α-subunits induces a right-sided shift of oxygen saturation that helps full dissociation of molecular oxygen from hemoglobin at the site of ischemia (Fig. 2).

Likewise the case of hemoglobin, differences between NO and CO in the heme structure in the β-subunit of sGC appear to cause distinct activation states of the catalytic α-subunit of the enzyme. Because of such a structural difference in the heme coordination between NO and CO, the interaction of the two gases on the prosthetic heme of the enzyme leads to a unique regulatory response of the enzyme: low tissue NO makes CO a modestly stimulatory modulator of the enzyme, whereas high tissue NO makes CO an inhibitory one (Suematsu and Ishimura, 2000). Observation that vascular smooth muscle cell-specific HO-1 transgenic mice exhibit systemic hypertension rather than hypotension supports such a possibility (Imai et al., 2001). This concept was also confirmed by our recent studies showing that the interactions between the two gases cause fine-tuning of the sGC function *in vivo* (Kajimura et al., 2002): we applied the monoclonal antibody (mAb) 3221 against sGC that can recognize the specific structure produced by the enzyme activation. Immunohistochemical analyses of rat retina where the background NO-generating activities appear heterogenous among different neuronal

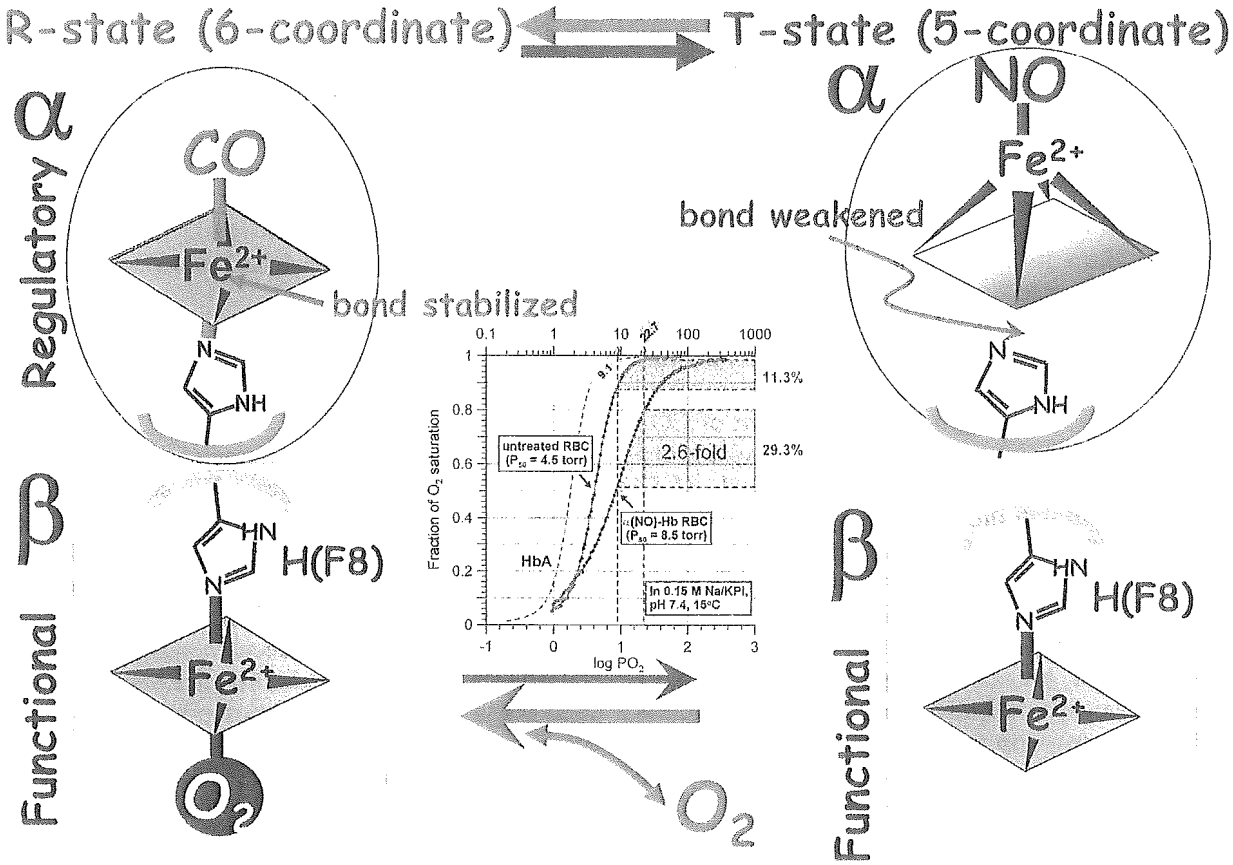

Fig. 2. Stabilization of hemoglobin allostery by CO and NO. R-state stabilization by binding CO to the α-subunit heme increases the affinity of molecular oxygen to the β-heme, while T-state stabilization by binding NO to the α-subunit decreases it. Note alterations in oxygen saturation curves in response to R- or T-state stabilization, indicating that CO and NO have distinct properties to alter protein function to each other. At the same time, T-state stabilization by NO serves as a possible therapeutic method to prepare erythrocytes with greater oxygen-delivering capacity.

layers revealed that light-induced up-regulation of HO-1 activates sGC in retinal pigment epithelia where NO seems low, while suppresses the enzyme in inner plexiform layer where NO is sufficiently generated. Distinct from NO, retina could benefit from the nonradical CO to maintain housekeeping cGMP without a risk of potential degradation of retinoids (Kajimura et al., 2002). Such a way to use CO is likely to to be the case in relaxation of hepatic stellate cells to guarantee sinusoidal patency or in apoptotic control of spermatogenesis, where vitamin A or NO-breakable DNA is abundantly stored, respectively (Ozawa et al., 2002).

HUNTING GASEOUS SIGNAL TRANSDUCERS BY METABOLOME ANALYSES

Since binding of gases to the prosthetic metal group of proteins depends on redox states of the metal *in vivo*, it is technically difficult to search for novel gas receptors using proteomics technology *in vitro*. We have recently attempted to apply metabolomics technology to look for such new receptors. Capillary electrophoresis combined with mass spectorometry (CE-MS) or liquid chromatography assisted by tandem mass spectorometry (LC-MS/MS) are powerful technologies that allow us to reveal differences in small molecular metabolites between control and disease conditions. Metabolome analyses is very powerful to examine specific metabolic pathways responsible for energy supply and oxidoreductive processes in bacteria that are distinct from those for mammals, as indicated by Tian and Nathan who identified roles of α-ketoglutarate decarboxylase in mycobacterium tuberculosis with our collaboration (Tian et al., 2005). We have also applied LC-MS/MS to examine alterations in sulfur-containing amino acids in cadmium-exposed rat testes where HO-1-CO is significantly upregulated in Leydig cells (Sugiura et al., 2005). In these experiments, the exposure to cadmium elicited an increase in substrates for remethylation pathway (e.g., methionine and S-adenosyl homocysteine and a decrease in cystathione, cysteine and H_2S, a novel gaseous mediator (Zhao et al., 2001). Such a local footprint of alterations in sulfur-containing amino acid metabolism among the landscape picture of metabolism led us to hypothesize that CO can inhibit cystathionine β synthase, a heme-containing rate-limiting enzyme for transsulfuration pathway; such a concept is consistent with observation that the purified enzyme with ferrous heme is sensitive to CO *in vitro* (Taoka and

Banerjee, 2001). Experimental models of liver diseases deserve further studies given evidence for significant biological effects of CO on the sulfur-containing amino acid metabolism, remethylation capacity and generation of glutathione and H_2S (Look et al., 2000. Robert et al., 2005).

ACKNOWLEDGMENTS

The authors acknowledge supports by 21st Century Center-of-Exellence Program and by Leading Project 17GS0419 for Biosimulation and Grant-in-Aid of Creative Science Research from the Ministry of Education, Sciences and Technology, and from NEDO in Japan.

REFERENCES

Abe K, Kimura H (1996) The possible role of hydrogen sulfide as an endogenous neuromodulator. J Neurosci 16:1066–1071.

Boyer JL, Klatskin G (1970) Canalicular bile flow and bile secretory pressure. Evidence for a non-bile salt dependent fraction in the isolated perfused rat liver. Gastroenterology 6:853–859.

Eto K, Ogasawara M, Umemura K, Nagai Y, Kimura H (2002) Hydrogen sulfide is produced in response to neuronal excitation. J Neurosci 22:3386–3391.

Fujii K, Sakuragawa T, Kashiba M, Sugiura Y, Kondo M, Maruyama K, Goda N, Nimura Y, Suematsu M (2005) Hydrogen sulfide as an endogenous modulator of biliary bicarbonate excretion in the rat liver. Antioxid Redox Signal 7:788–794.

Goda N, Suzuki K, Naito M, Takeoka S, Tsuchida E, Ishimura Y, Tamatani T, Suematsu M (1998) Distribution of heme oxygenase isoforms in rat liver. Topographic basis for carbon monoxide-mediated microvascular relaxation. J Clin Invest 101:604–612.

Hayashi S, Takamiya R, Yamaguchi T, Matsumoto K, Tojo SJ, Tamatani T, Kitajima M, Makino N, Ishimura Y, Suematsu M (1999) Induction of heme oxygenase-1 suppresses venular leukocyte adhesion elicited by oxidative stress: role of bilirubin generated by the enzyme. Circ Res 85:663–671.

Imai T, Morita T, Shindo T, Nagai R, Yazaki Y, Kurihara H, Suematsu M, Katayama S (2001) Vascular smooth muscle cell-directed overexpression of heme oxygenase-1 elevates blood pressure through attenuation of nitric oxide-induced vasodilation in mice. Circ Res 89:55–62.

Kajimura M, Shimoyama M, Tsuyama S, Suzuki T, Kozaki S, Takenaka S, Tsubota K, Oguchi Y, Suematsu M (2002) Visualization of gaseous monoxide reception by soluble guanylate cyclase. FASEB J 17:506–508.

Kashiwagi S, Kajimura M, Yoshimura Y, Suematsu M (2002) Nonendothelial source of nitric oxide in arterioles but not in venules: Alternative source revealed in vivo by diaminofluorescein microfluorography. Circ Res 91:E55–E64.

Kato Y, Shimazu M, Kondo M, Uchida K, Kumamoto Y, Wakabayashi G, Kitajima M, Suematsu M (2003) Bilirubin rinse: A simple protectant against the rat liver graft injury mimicking heme oxygenase-1 preconditioning. Hepatology 38:364–373.

Kyokane T, Norimizu S, Taniai H, Yamaguchi T, Takeoka S, Tsuchida E, Naito M, Nimura Y, Ishimura Y, Suematsu M (2001) Carbon monoxide from heme catabolism protects against hepatobiliary dysfunction in endotoxin-treated rat liver. Gastroenterology 120:1227–1240.

Look MP, Riezler R, Reichel C, Brensing KA, Rockstroh JK, Stabler SP (2000) Is the increase in serum cystathionine levels in patients with liver cirrhosis a consequence of impaired homocysteine transsulfuration at the level of gamma-cystathionase? Scand J Gastroenterol 35:866–872.

Makino N, Suematsu M, Sugiura Y, Morikawa H, Shiomi S, Goda N, Sano T, Nimura Y, Sugimachi K, Ishimura Y (2001) Altered expression of heme oxygenase-1 in the livers of patients with portal hypertensive diseases. Hepatology 33: 32–42.

Mori M, Suematsu M, Kyokane T, Sano T, Suzuki H, Yamaguchi T, Ishimura Y, Ishii H (1999) Carbon monoxide-mediated alterations in paracellular permeability and vesicular transport in acetaminophen-treated perfused rat liver. Hepatology 30:160–168.

Motterlini R, Gonzales A, Foresti R, Clark JE, Green CJ, Winslow RM (1998) Heme oxygenase-1-derived carbon monoxide contributes to the suppression of acute hypertensive responses in vivo. Circ Res 83:568–577.

Norimizu S, Kudo A, Kajimura M, Ishikawa K, Taniai H, Yamaguchi T, Fujii K, Arii S, Nimura Y, Suematsu M (2003) Carbon monoxide stimulates mrp2-dependent excretion of bilirubin-IXα into bile in the perfused rat liver. Antioxid Redox Signal 5:449–456.

Otterbein LE, Bach FH, Alam J, Soares M, Tao Lu H, Wysk M, Davis RJ, Flavell RA, Choi AM (2000) Carbon monoxide has anti-inflammatory effects involving the mitogen-activated protein kinase pathway. Nat Med 6:422–428.

Otterbein LE, Zuckerbaun BS, Haga M, Liu F, Song R, Usheva A, Stachulak C, Bodyak N, Smith RN, Csizmadia E, Tyagi S, Akamatsu Y, Flavell RJ, Billiar TR, Tzeng E, Bach FH, Choi AM, Soares MP (2003) Carbon monoxide suppresses arteriosclerotic lesions associated with chronic graft rejection and with balloon injury. Nat Med 9:183–190.

Ozawa N, Goda N, Makino N, Yamaguchi T, Yoshimura Y, Suematsu M (2002) Leydig cell-derived heme oxygenase-1 regulates apoptosis of premeiotic germ cells in response to stress. J Clin Invest 109:457–467.

Robert K, Nehme J, Bourdon E, Pivert G, Friguet B, Delcayre C, Delabar JM, Janel N (2005) Cystathionine beta synthase deficiency promotes oxidative stress, fibrosis and steatosis in mice liver. Gastroenterology 128:1405–1415.

Sano T, Shiomi M, Wakabayashi Y, Shinoda Y, Goda N, Yamaguchi T, Nimura Y, Ishimura Y, Suematsu M (1997) Endogenous carbon monoxide suppression stimulates bile acid-dependent biliary transport in perfused rat liver. Am J Physiol 272: G1268–G1275.

Shinoda Y, Suematsu M, Wakabayashi Y, Suzuki T, Goda N, Saito S, Yamaguchi T, Ishimura Y (1998) Carbon monoxide as a regulator of bile canalicular contractility in cultured rat hepatocytes. Hepatology 28:286–295.

Shiomi M, Wakabayashi Y, Sano T, Shinoda Y, Nimura Y, Ishimura Y, Suematsu M (1998) Nitric oxide suppression reversibly attenuates mitochondrial dysfunction and cholestasis in endotoxemic rat liver. Hepatology 27:108–115.

Suematsu M, Kashiwagi S, Sano T, Goda N, Shinoda Y, Ishimura Y (1994) Carbon monoxide as an endogenous modulator of hepatic vascular perfusion. Biochem Biophys Res Commun 205:1333–1337.

Suematsu M, Goda N, Sano T, Kashiwagi S, Egawa T, Shinoda Y, Ishimura Y (1995) Carbon monoxide: an endogenous modulator of sinusoidal tone in the perfused rat liver. J Clin Invest 96:2431–2437.

Suematsu M, Ishimura Y (2000) The heme oxygenase-carbon monoxide system: A regulator of hepatobiliary function. 31:3–6.

Suganuma K, Tsukada K, Kashiba M, Tsuneshige A, Goda N, Kitajima M, Yonetani T, Suematsu M (2005) Erythrocytes with T-state-stabilized hemoglobin as a therapeutic tool for post-ischemic liver dysfunction. Antioxid Redox Signal, in press.

Sugiura Y, Kashiba M, Maruyama K, Hoshikawa K, Sasaki R, Saito K, Kimura H, Goda N, Suematsu M (2005) Cadmium exposure alters metabolomics of sulfur-containing amino acids in rat testes. Antioxid Redox Signal 7:781–787.

Taoka S, Banerjee R (2001) Characterization of NO binding to human cystathionine beta synthase. J Inorg Biochem 87:245–251.

Tian J, Bryk R, Itoh M, Suematsu M, Nathan C (2005) Variant tricarboxylic acid cycle in Mycobacterium tuberculosis: Identification of α-ketoglutarate decarboxylase. Proc Natl Acad Sci U S A 102:10670–10675.

Trauner M, Nathanson MH, Rydberg SA, Koeppel TA, Gartung C, Sessa WC, Boyer JL (1997) Endotoxin impairs biliary glutathione and HCO_3^- excretion and blocks the choleretic effect of nitric oxide in rat liver. Hepatology 25:1184–1191.

Verma A, Hirsh DJ, Glatt CE, Ronnett GV, Snyder SH (1993) Carbon monoxide: a putative neural messenger. Science 259:381–384.

Wakabayashi Y, Takamiya R, Mizuki A, Kyokane T, Goda N, Yamaguchi T, Takeoka S, Tsuchida E, Suematsu M, Ishimura Y (1999) Carbon monoxide overproduced by heme oxygenase-1 causes a reduction of vascular resistance in perfused rat liver. Am J Physiol Gastrointest Liver Physiol 277:G1088–G1096.

Yamaguchi T, Wakabayashi Y, Tanaka M, Sano T, Ishikawa H, Nakajima H, Suematsu M, Ishimura Y (1996) Taurocholate induces directional excretion of bilirubin into bile in perfused rat liver. Am J Physiol Gastrointest Liver Physiol 270:G1028–G1032.

Yonetani T, Tsuneshige A, Zhou Y, Chen X (1998) Electron paramagnetic resonance and oxygen binding studies of α-nitrosyl hemoglobin. J Biol Chem 273:20323–20333.

Zhao W, Zhang J, Lu Y, Wang R (2001) The vasorelaxant effect of H_2S as a novel endogenous gaseous K_{ATP} channel opener. EMBO J 20: 6008–6016.

J Appl Physiol 96: 1561–1568, 2004.
First published December 5, 2003; 10.1152/japplphysiol.00764.2003.

HIGHLIGHTED TOPIC | *Oxygen Sensing in Health and Disease*

Red blood cell velocity and oxygen tension measurement in cerebral microvessels by double-wavelength photoexcitation

Kosuke Tsukada,[1] Eiichi Sekizuka,[2] Chikara Oshio,[3] Katsuhiko Tsujioka,[1] and Haruyuki Minamitani[4]
[1]*Department of Physiology, Kawasaki Medical School, Kurashiki, 701-0192;*
[2]*Department of Clinical Research, National Saitama Hospital; Wako, 351-0102;* [3]*Oshio Clinic, Chiyoda-ku, 101-0063; and* [4]*Department of Applied Physics and Physico-Informatics, Faculty of Science and Technology, Keio University, Yokohama, 223-8522 Japan*

Submitted 23 July 2003; accepted in final form 2 December 2003

Tsukada, Kosuke, Eiichi Sekizuka, Chikara Oshio, Katsuhiko Tsujioka, Haruyuki Minamitani. Red blood cell velocity and oxygen tension measurement in cerebral microvessels by double-wavelength photoexcitation. *J Appl Physiol* 96: 1561–1568, 2004. First published December 5, 2003; 10.1152/japplphysiol.00764.2003.—Because the regulation of microcirculation in the cerebral cortex cannot be analyzed without measuring the blood flow dynamics and oxygen concentration in cerebral microvessels, we developed a fluorescence and phosphorescence system for estimating red blood cell velocity and oxygen tension in cerebral microcirculation noninvasively and continuously with high spatial resolution. Using red blood cells labeled with fluorescent isothiocyanate to visualize red cell distribution and using the oxygen quenching of Pd-meso-tetra-(4-carboxyphenyl)-porphyrin phosphorescence to measure oxygen tension enabled simultaneous measurement of blood velocity and oxygen tension. We examined how the measurement accuracy was affected by the spatial resolution and by the excitation laser light passing through the targeted microvessel and exciting the oxygen probe dye in the tissue beneath it. Focusing the excitation light into the microvessel stabilized the phosphorescence lifetime at each spatial resolution; moreover, it greatly reduced phosphorescence from the brain tissue. Animal experiments involving acute hemorrhagic shock demonstrated the feasibility of our system by showing that the changes in venular velocity and oxygen tension are synchronized to the change in mean arterial pressure. Our system measures the red cell velocity and oxygen concentration in the cerebral microcirculation by using the differences in luminescence and wavelength between fluorescence and phosphorescence, making it possible to easily acquire information about cerebral microcirculatory distribution and oxygen tension simultaneously.

cerebral microcirculation; erythrocyte velocity; oxygen tension; fluorescence; phosphorescence

THE CEREBRAL NERVE CELLS ARE extremely vulnerable to ischemia because they store hardly any oxygen or substrates. Because higher brain function therefore depends on the microcirculation, the brain is expected to have a strong autoregulation maintaining the local blood flow and volume. Consequently, an extremely effective way to study the regulation of the microcirculation in the cerebral cortex is by measuring the dynamics of the cerebral microcirculation while simultaneously measuring the oxygen concentration in the cerebral microvessels.

When one measures the microcirculatory blood flow in two-dimensional structures such as dorsal skin, the mesentery or cremaster muscle, the cheek pouches of hamsters, and the ears of rabbits, one can observe these structures under transmitted illumination. Although the microcirculation in the brain cortex cannot be observed under transmitted illumination, the dynamics of the blood flow distribution can be visualized by using FITC-labeled red blood cells (RBCs) and an incident-light fluorescence microscope, as described by Ishikawa et al. (3). On the other hand, the oxygen electrodes often used when measuring oxygen tension in vivo cannot be used in microvessels because they physically damage them too much and because their spatial resolution is inadequate. The partial pressure of oxygen in organs must therefore be measured by a noncontact, noninvasive method. The oxygen tension can be measured in vivo by using the changes in the lifetime of phosphorescence emitted from a porphyrin dye, as reported (12, 22), and this technique is being established as an alternative method for measuring the oxygen tension in organs.

In the present study, we used fluorescently labeled RBCs to visualize blood flow and used the phosphorescence decay method to measure oxygen tension. By exciting two dyes with two different wavelengths, both RBC velocity and oxygen tension could be measured continuously, but we had to ensure that the absorption and emission spectra of the fluorescence dye used for visualizing RBC flow and the phosphorescence dye used for measuring oxygen tension did not overlap. In addition, we had to determine how the measurement accuracy was affected by excitation light passing through the targeted microvessel and exciting the oxygen probe dye in the brain tissue beneath it.

The aim of this study was to develop a fluorescence and phosphorescence system that can simultaneously measure the cerebral microcirculatory distribution and the oxygen tension in cerebral microvessels. We examined the emission and absorption spectra of fluorescence and phosphorescence dyes, the spatial resolution, the half-life of probe dye in blood, the extravasation of the dye, and the phosphorescence emission from the tissue lying under the targeted microvessels. To demonstrate the feasibility of our system, we performed animal experiments involving acute hemorrhagic shock.

Address for reprint requests and other correspondence: K. Tsukada, Dept. of Physiology, Kawasaki Medical School, 577 Matsushima, Kurashiki, Okayama 701-0192 Japan (E-mail: ktsukada@med.kawasaki-m.ac.jp).

The costs of publication of this article were defrayed in part by the payment of page charges. The article must therefore be hereby marked "*advertisement*" in accordance with 18 U.S.C. Section 1734 solely to indicate this fact.

MATERIALS AND METHODS

Animal preparations. All animals received humane care in compliance with the "Guide for the Care and Use of Laboratory Animals" prepared by the Animal Research Committee of the Kawasaki Medical School. Male Wistar rats weighing 300–350 g were anesthetized with an intraperitoneal injection of α-chloralose (60 mg/kg) and urethane (600 mg/kg). The head of each rat was fixed in a stereotaxic frame, and the left parietal bone was exposed by a longitudinal midline skin incision. After three polyethylene tubes (PE-50) were fixed to the skull with cyanoacrylate, a craniectomy was performed, and a closed cranial window (5 mm in diameter) was made using a cover glass and a rubber O-ring. Artificial cerebrospinal fluid consisting of 147.8 meq/l Na^+, 3.0 meq/l K^+, 2.3 meq/l Mg^{2+}, 2.3 meq/l Ca^{2+}, 135.2 meq/l Cl^-, 19.6 meq/l HCO_3^-, 1.7 meq/l lactate, 1.1 mM phosphate, and 3.9 mM glucose was superfused at 0.1 ml/min. A thermistor with a diameter of 2.3 mm was fitted to the cranial window to monitor the temperature, and the cerebral fluid was maintained at 37°C. The left femoral artery was cannulated for monitoring the mean arterial blood pressure (MAP), the right femoral artery was cannulated for withdrawing blood, and the right femoral vein was cannulated for infusing blood or drugs.

Probe administration for RBC flow visualization and oxygen measurement. The RBC flow in cerebral microvessels was visualized by perfusing RBCs labeled with fluorescent isothiocyanate (FITC, Sigma Chemical) as described by Ishikawa et al. (3). Blood was withdrawn from the donor rat, and the RBCs were centrifuged and washed. The FITC was excited by irradiating it at an energy density of 5 mW/cm^2 with the light from a mercury lamp and passing it through a band-pass filter (450–490 nm). Each rat received 0.1 ml of FITC-labeled RBC suspension injected into its cannulated femoral vein. (This amount of FITC-labeled RBCs accounted for ~1/50 of all the RBCs in the body.)

Image processing of fluorescent blood flow. Figure 1 shows a block diagram of the system used for measuring RBC velocity, vessel diameter, and oxygen tension in individual microvessels of the cerebral cortex. Microscopic images made with the FITC-emitted light that had passed through a long-pass filter (>520 nm) were recorded with a charge-coupled device camera equipped with an image intensifier (C6653MOD, Hamamatsu Photonics). The images were processed automatically by using a previously developed system (21). Briefly, this system consists of a host computer, a Hi8 video recorder, and an image-data-processing board. One frame of a still image can be viewed on the monitor via the image-processing board, which takes two still 512 × 512-pixel images, and the intensity can be digitized to 256 levels. Automated velocity measurement was made possible by writing C-language sequences to load the images into memory, calculate the correlation, fast-forward through the video frames, and so on.

Oxygen tension measurement using phosphorescence decay. The Pd-meso-tetra-(4-carboxyphenyl)-porphyrin (Pd-TCPP, Porphyrin Products) used as the phosphorescent probe for the O_2-dependent quenching was dissolved (20 mg/ml) in physiological saline containing bovine serum albumin and buffered to a pH of 7.4 with phosphate buffer. Each rat received a bolus of Pd-TCPP (30 mg/kg) through a slow intravenous injection, and the Pd-TCPP in the microvessels was excited by using the second harmonic of a Q-switched Nd:YAG pulse laser (532-nm wavelength, 6-ns pulse width at half maximum, 1-Hz pulse recurrence frequency, 200-nJ/pulse irradiation energy) through the objective lens of a microscope. Phosphorescence passing through a long-pass filter (>620 nm) was detected with a photomultiplier tube (PMT) (R1894, Hamamatsu Photonics). The voltage signal (current signal converted with resistance of 50 kΩ) from the PMT was fed into a personal computer via an analog-to-digital converter (NR-2000, Keyence) with a sampling frequency of 200 kHz and a sampling number of 500 points. When the decay signal was processed for use in calculating the phosphorescence lifetime, the first 10 sampling points (corresponding to 50 μs) from the start of sampling were excluded because they included the intensity of the exciting laser

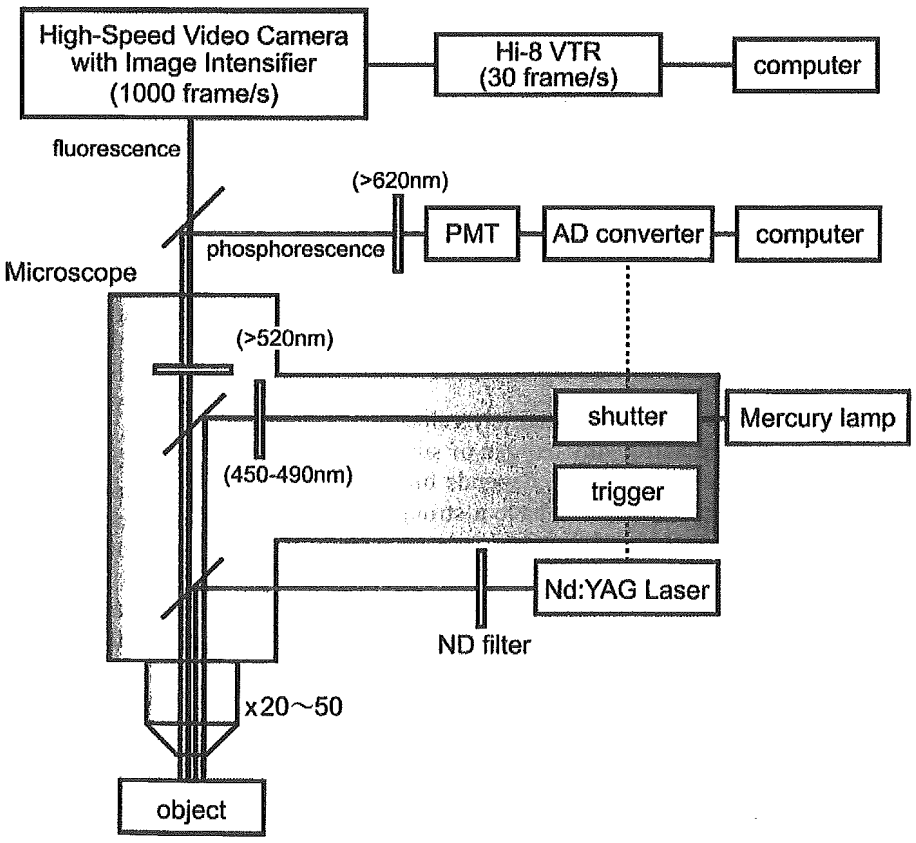

Fig. 1. Block diagram of system used for measuring red blood cell (RBC) flow velocity and oxygen tension in cerebral microvessels. To irradiate FITC for visualizing flow distribution and Pd-meso-tetra-(4-carboxyphenyl)-porphyrin (Pd-PCPP) for measuring oxygen tension alternately, a mechanical shutter was used to control the output of a mercury lamp and the signal from a limit switch was used to trigger an Nd:YAG laser when the shutter was closed. Blood flow images recorded with a charge-coupled device camera were used to automatically measure flow velocity by computer. PMT, photomultiplier tube; VTR, video tape recorder; AD, analog to digital; ND, neutral density.

light, which was not completely blocked by the long-pass filter. In addition, <1% of the maximum intensity of the PMT signal was rejected to reduce the contribution of dark current generated by the PMT. Phosphorescence lifetime τ was obtained by least-squares fitting of the remaining data to a single exponential curve. The oxygen tension (P_{O_2}) was calculated from the Stern-Volmer equation

$$I_0/I = \tau_0/\tau = 1 + k_q \cdot \tau_0 \cdot P_{O_2} \quad (1)$$

where I_0 and τ_0 are phosphorescence intensity and lifetime in the absence of oxygen, I and τ are the intensity and lifetime at a given oxygen tension, and k_q is the rate constant of oxygen quenching. The k_q and τ_0 values for our system were obtained from a calibration experiment using oxygen electrodes; at 37°C with a pH of 7.4 they were 374 $Torr^{-1} \cdot s^{-1}$ and 0.74 ms.

Irradiation timing of two light sources. To obtain two physiological values, the cerebral microcirculatory blood flow distribution and oxygen tension, we had to alternately irradiate each of two dyes in a targeted microvessel with the light from two excitation light sources. To measure the RBC velocity and oxygen tension at 1 Hz, we used a mechanical shutter to control the output of a mercury lamp and used the signal from a limit switch to trigger an Nd:YAG laser when the shutter was closed. The irradiation times of the laser and mercury lamp were, respectively, 6 ns and 300 ms.

Estimation of Pd-TCPP concentration in blood plasma. After five rats received 30 mg/kg of Pd-TCPP in solution (20 mg/ml) by slow injection into the femoral vein, blood samples were removed from the postcaval vein with a heparinized syringe at 5 and 30 min and at 1, 3, and 6 h. The plasma was extracted by centrifuging the samples at 1,500 rpm for 15 min; the skimming fluid taken as a measurement sample was obtained by additional centrifugation at 1,000 rpm for 5 min. The Pd-TCPP concentration in the plasma sample was quantified by absorption spectrophotometry, using the relation between absorbance and concentration previously calibrated at Pd-TCPP concentrations of 0.50, 0.25, 0.13, and 0.06 mg/ml (data not shown).

Narrow capillary model. Because the spatial resolution depends on the diameter of the laser spot, the effect of the spot size on lifetime was determined by changing the objective lens of the microscope. A narrow glass capillary with a 410-μm outer diameter and a 350-μm inner diameter was used as a microvessel model; it was set in a cranial window made by using the same materials and conditions as for the in vivo experiments. A solution of Pd-TCPP deoxygenized with sodium sulfite was kept at 37°C and a pH of 7.4 and perfused through the glass capillary. The phosphorescence intensity and lifetime were measured at different resolutions (i.e., spot sizes) by changing the magnification of the objective lens (×20 or ×50).

Flushing blood from microvessels. To photoexcite Pd-TCPP defused into extravascular cerebral tissue (i.e., not in microvessels), we inserted a catheter tube 0.8 mm in diameter into the left common carotid artery in the direction of the middle cerebral artery, and we fixed the edge of the tube at the internal carotid artery. After preparing the closed cranial window on the left parietal bone and administering the Pd-TCPP, we left the rat for 1 h so that the Pd-TCPP had sufficient time to leak from the microvessels into the extravascular tissue. Then, while applying continuous laser irradiation to a venule, we gave the rat an overdose of pentobarbital sodium, reducing both the MAP and heart rate to 0. Physiological saline was immediately infused via a carotid artery, flushing the blood and Pd-TCPP from the microvessels, and the targeted microvessel was observed with a microscope to verify that it was filled with saline. The phosphorescence emission from the Pd-TCPP that had leaked into the tissue was measured at a constant laser power before and after the flush.

Acute hemorrhagic shock model. Four rats were put into acute hemorrhagic shock by letting them bleed from a catheter in the femoral artery. They were bled, at 7–8 ml/min, to a MAP of 40 mmHg in <1 min. The shed blood was collected in heparinized syringes and kept at 37°C. The MAP was maintained at 40 ± 3 mmHg for 5 min by intermittently withdrawing 0.3–0.4 ml of blood. After the period of shock, the rats were resuscitated by infusing autologous whole blood.

RESULTS

Absorption and emission spectrum of FITC and Pd-TCPP. The absorption and emission spectra of the FITC used for labeling the RBCs and Pd-TCPP used as the oxygen-sensitive probe are shown in Fig. 2. For RBC velocity and oxygen tension to be measured simultaneously, the Pd-TCPP absorption must be extremely small in the wavelength band used to excite the FITC (from 460 to 490 nm). The Q-band of the Pd-TCPP was observed near 532 nm, which is the wavelength of the second harmonic of the Nd:YAG laser.

Simultaneous measurement of RBC velocity and oxygen tension. Figure 3*A* shows the microcirculatory vessel structure in the cerebral cortex observed in the closed cranial window. Figure 3*B* shows a high-magnification blood flow image with FITC-labeled RBCs. Figure 3*C* shows an image of laser light irradiating a targeted microvessel to measure the oxygen tension in the vessel. The RBC velocity and oxygen tension were

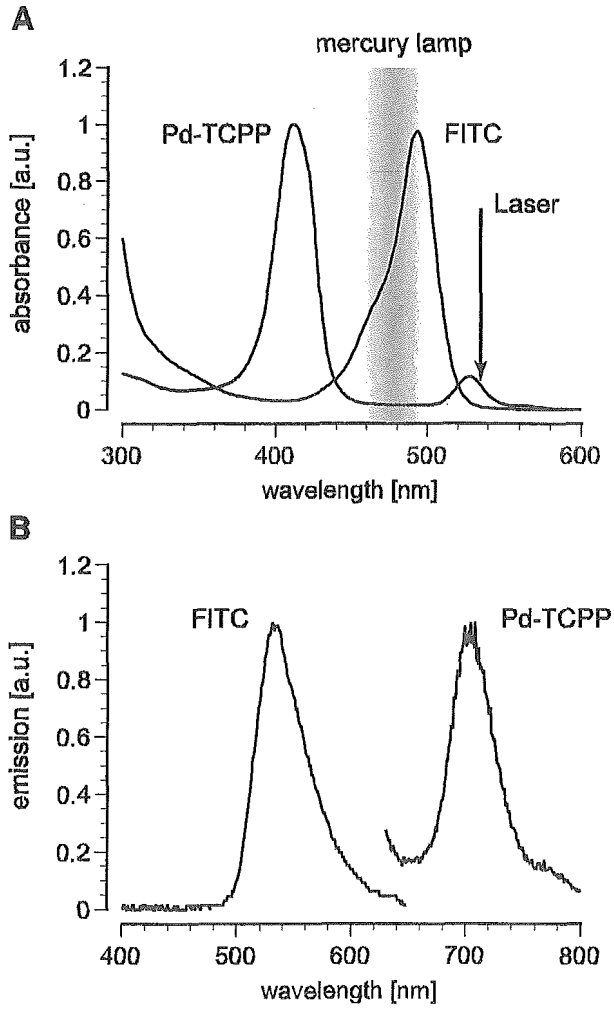

Fig. 2. Absorption (*A*) and emission (*B*) spectra of FITC used for labeling RBCs and Pd-TCPP used as oxygen-sensitive probes. Pd-TCPP absorption was extremely small in the band exciting the FITC (from 460 to 490 nm), and FITC absorption was small at the 532-nm wavelength exciting the Pd-TCPP. a.u., Arbitrary units.

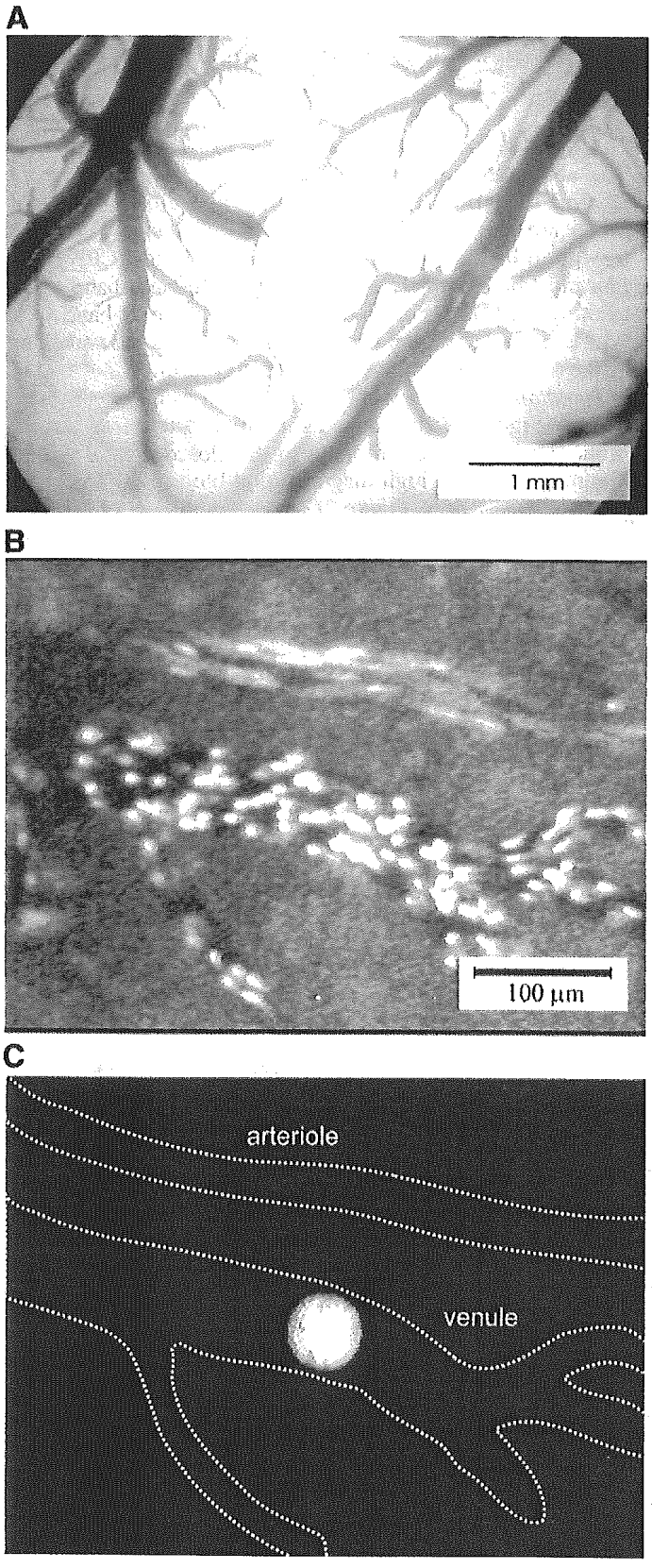

Fig. 3. Microscopic images of cerebral microvessel structure observed in closed cranial window (*A*), high-magnification blood flow of cerebral microcirculation visualized with FITC-labeled RBCs (estimated to be ~2% of all circulating RBCs) (*B*), and image of laser light irradiating a targeted microvessel to measure oxygen tension (*C*). Irradiation times of mercury lamp in *B* and laser in *C* were, respectively, 300 ms and 6 ns.

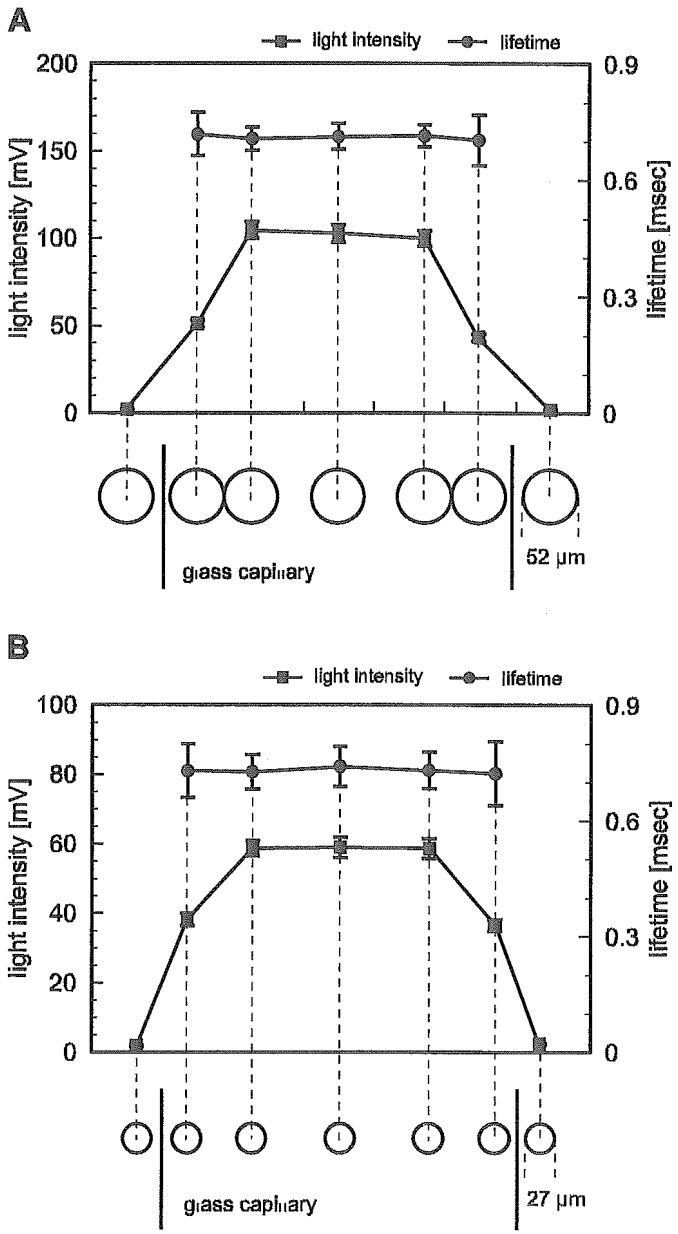

Fig. 4. Effect of laser spot size on measurement accuracy was small. Laser spot diameter, 52 (*A*) and 27 μm (*B*), i.e., the spatial resolution, was determined by magnification of objective lens: ×20 (*A*) and ×50 (*B*). A narrow glass capillary tube with a 410-μm outer diameter and a 350-μm inner diameter was filled with Pd-TCPP solution and used as a microvessel model. Even when the phosphorescence intensity was lower for spots near the wall, the lifetime was not affected at either resolution, indicating that stable oxygen measurement can be obtained by irradiating the inside of the microvessel. Values are means ± SD for 20 laser irradiations.

measured alternately at 1 Hz by using the shutter installed in the microscope to change between the two light sources (Nd: YAG laser and mercury lamp). After a microvessel was chosen for measurement, the microscope stage was positioned so as to direct the laser into the targeted vessel.

Spatial resolution. The phosphorescence intensity and lifetime at various locations in a glass capillary under different laser spots are shown in Fig. 4, *A* and *B*. Values are expressed as means ± SD for 20 laser irradiations. The phosphorescence lifetimes at the center were 0.72 ± 0.03 and 0.74 ± 0.05 ms

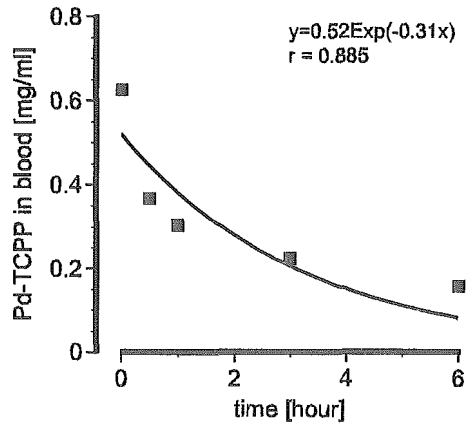

Fig. 5. Blood concentration curve obtained after bolus injection of Pd-TCPP. Leakage of Pd-TCPP from microvessels to extravascular tissue was observed. Fitting this data to an exponential decay curve yielded the equation $y = 0.52 \exp(-0.31x)$, $r = 0.885$, and 2.23 h for the half-life of Pd-TCPP in blood.

with ×20 and ×50 magnification, which was almost equivalent to τ_0. The laser spot, as measured from the irradiated images, was ~52 and 27 μm in diameter with objective lenses with ×20 and ×50 magnification, respectively. The phosphorescence lifetime remained about the same, even though the intensity decreased as the spot approached the wall because the amount of irradiated Pd-TCPP near the capillary wall was less than at the center in the *Z*-axial direction.

Pd-TCPP half-life in blood. Figure 5 shows the blood concentration after bolus injection of Pd-TCPP. Five minutes after the injection, the plasma concentration of Pd-TCPP was 624.7 μg/ml. At 0.5, 1, 3, and 6 h, the concentrations were, respectively, 366.2, 302.5, 222.2, and 155.7 μg/ml. Fitting this data to an exponential decay curve yielded 2.23 h for the half-life of Pd-TCPP in blood.

Phosphorescence emission from cerebral tissue after flushing blood from microvessels. Figure 6, *A* and *B*, shows, respectively, the decay curves of the phosphorescence before and after flushing the blood from the microvessels, and Fig. 6, *C* and *D*, shows, respectively, the log-intensity plots of the data in *A* and *B*. After the subject rat was killed, the oxygen tension calculated from the phosphorescence decay curves, obtained both before and after flushing, was 0.9 Torr. Correlation coefficient r^2 for the data in the valid area could be fitted to a single exponential function (0.998), suggesting that phosphorescence decay can be detected with high sensitivity and that lifetime can be calculated with high accuracy. In contrast, the phosphorescence intensity from the microvessel from which Pd-TCPP had been flushed with physiological saline was

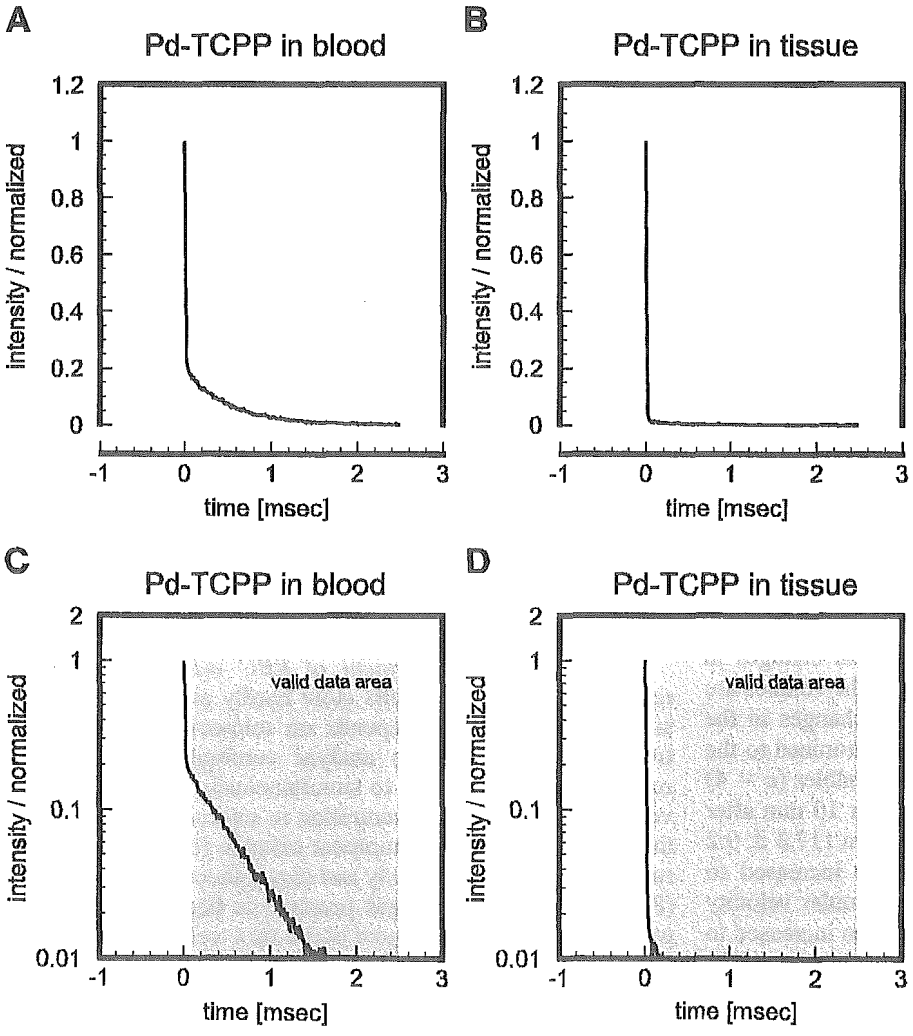

Fig. 6. Phosphorescence emission from Pd-TCPP in tissue was estimated by irradiating microvessels with a laser beam after flushing the blood from them. *A* and *B*: decay curves of phosphorescence before and after flushing. *C* and *D*: log-intensity plots of the data shown in *A* and *B*. Decay signals used for calculating oxygen tension were taken from "valid data areas" in *C* and *D*.

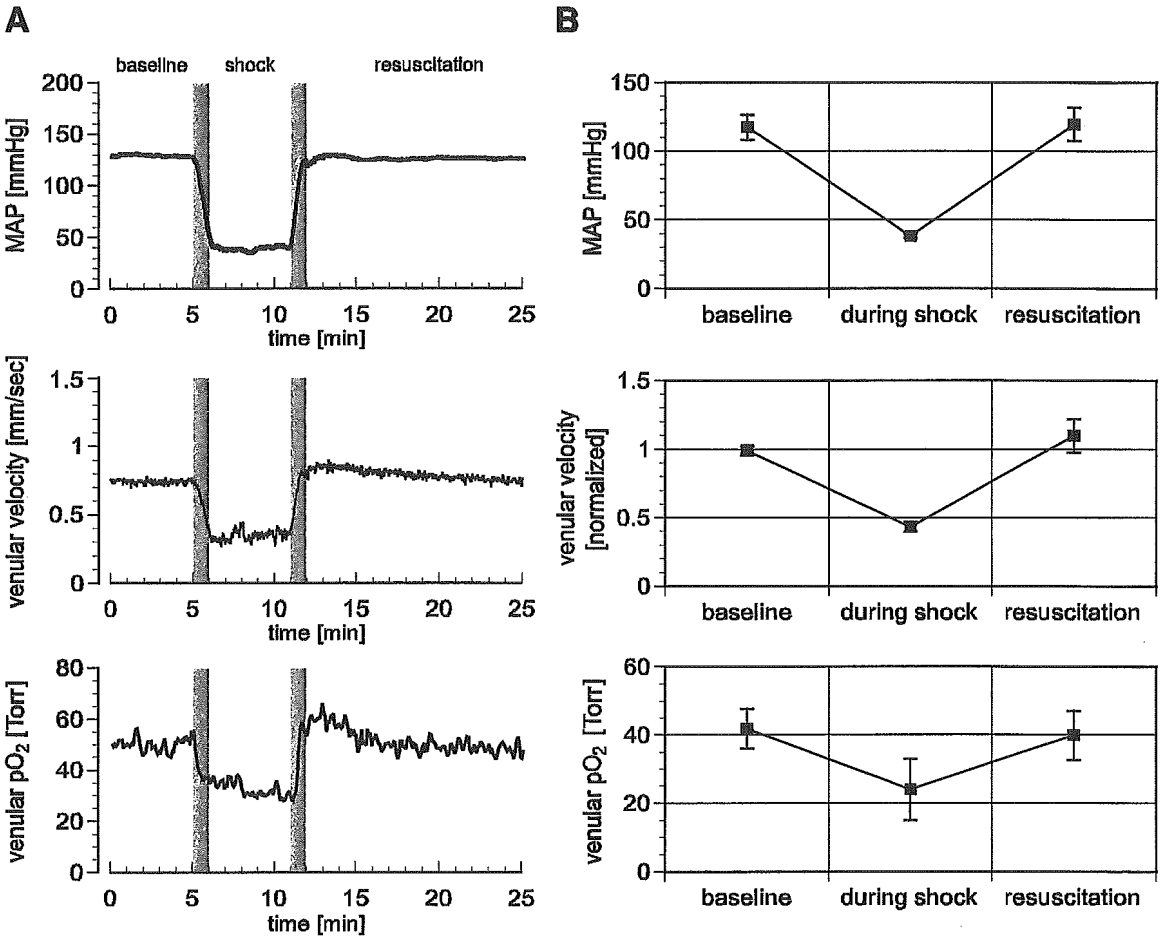

Fig. 7. Typical changes in mean arterial blood pressure (MAP), RBC velocity, and oxygen tension in venules during acute hemorrhagic shock. Blood was bled from a catheter in the femoral artery until the arterial pressure reached a mean of 40 mmHg; after the rats entered a period of shock, they were resuscitated by infusing autologous whole blood. Gray bars in *A* indicate the periods of bleeding and infusing blood. The average ± SD values of these variables (n = 4) before bleeding (baseline), during shock, and for 10 min after resuscitation are shown in *B*.

greatly reduced. As described above, the valid data for calculating the phosphorescence lifetime are the data gathered starting 50 μs after data acquisition. The greatest phosphorescence intensity (voltage signal from PMT) in this range was 15.4 mV in blood (Fig. 6*A*) and 1.9 mV in tissue (Fig. 6*B*). And shown in Fig. 6*D*, the sampling signal in the valid data area was extremely low, suggesting that there was very little phosphorescence emission from the extravascular tissue.

Hemorrhagic shock and resuscitation. Typical changes in the MAP, RBC velocity, and oxygen tension in the venules are shown in Fig. 7*A*, where we can see that the changes in the venular velocity and oxygen tension were synchronized to the change in MAP. The average values of these variables (n = 4) before bleeding (baseline), during shock, and for 10 min after resuscitation are shown in Fig. 7*B*. MAP fell from 117.3 ± 9.2 to 38.2 ± 1.4 mmHg during shock and then increased to 119.3 ± 11.9 mmHg after resuscitation. The venular velocity dropped to 43 ± 4% of its baseline value and then increased to 110 ± 12% of its baseline value. The venular oxygen tension fell from 41.9 ± 5.8 to 24.0 ± 9.0 Torr and then increased to 40.0 ± 7.2 Torr.

DISCUSSION

We set up and evaluated the effectiveness of our optical system for measuring the RBC velocity and oxygen tension in cerebral microcirculation simultaneously and continuously by using the difference in wavelength and luminescence between fluorescence and phosphorescence. We also examined factors affecting the accuracy of our phosphorescence photometry measurements through in vitro experiments.

Simultaneous measurement of RBC velocity and oxygen tension. Because brain cells store hardly any oxygen or substrates, brain function depends on microcirculation. An extremely efficient way to analyze cerebral microcirculatory regulation would thus be to simultaneously measure the RBC velocity and oxygen concentration in microregions. However, there is no convenient equipment suitable for measuring these two parameters continuously and simultaneously. Liss and Liss (8) monitored tissue oxygen pressure in flap microcirculation with electrodes and measured blood flow velocity by using the laser-Doppler method. In macroscopic measurement of tissue oxygenation, these techniques are probably easy to use. With regard to measurement in microcirculation, Parthasarathi and

Lipowsky (9) used oxygen electrodes to measure the oxygen in rat cremaster muscle and used the two-slit technique to measure blood flow in the muscle. Although oxygen electrodes can be used to measure the oxygen tension in various types of tissue, they cannot be used in blood vessels (especially microvessels) because their use requires physical invasion. The phosphorescence decay method using the photochemical reaction between porphyrin dye and oxygen molecules makes it possible to measure oxygen tension noninvasively, to obtain the local oxygen concentration with high spatial resolution, and to obtain the absolute partial pressure instead of a relative value.

Systems based on phosphorescence decay can be roughly divided into two types: those that can be used to draw oxygen mappings and those that can provide one-point measurements suitable for microcirculation study. The former type has been applied to kidney (11), liver (25), the carotid body (7), cells (10), and brain (24) and has also been used in ophthalmology (16) and in cancer studies (23). Shonat et al. (15) imaged hemoglobin saturation and oxygen tension in the cerebral cortex of mice. The latter type can be used to measure the local oxygen tension in tissue or in microvessels by focusing excitation light through the objective lens of a microscope (1, 2, 6, 13, 18). Kerger, Tsai, and colleagues (5, 19, 20) applied it and used the photodiode correlation method to measure blood velocity in dorsal skin microcirculation while using originally developed equipment to measure the diameter of the microvessels. As explained in the introduction, however, when researchers needed to measure both RBC velocity and oxygen tension, they were restricted to two-dimensional tissue samples.

As shown in Fig. 7, both venular velocity and oxygen tension in microvessels were synchronized to changes in blood pressure. The phosphorescence decay method has been used to evaluate the physiological reactions in certain organs during hemorrhagic shock (4, 14). Song et al. (17) reported deterioration in the oxygen tension in cortical tissue caused by hemorrhagic hypotension and recovery with PEG solution in piglet brain, and Yonetani et al. (26) reported a decrease in the cortical oxygen pressure with decreasing arterial pressure. However, quantified oxygen fluctuation with changes in the microcirculatory distribution in the cerebral cortex has not been reported.

Measurement accuracy and spatial and time resolution. As shown in Fig. 4, the phosphorescence lifetime was stable at each resolution when the laser spot was inside the targeted microvessel, even when the phosphorescence intensity decreased. This indicates that measurements should be stable if the phosphorescence lifetime is stable, even if the phosphorescence intensity decreases because of a decrease in Pd-TCPP in the blood. Also, as shown in Fig. 4, the spatial resolution increased when the magnification was increased, meaning that the measurement of the true capillaries is theoretically possible (27). However, increasing the magnification reduces the volume of phosphorescent light received, and, in the case of true capillaries, the volume of Pd-TCPP in the vessels also decreases, so measurement accuracy drops noticeably, meaning that the noise and the error rate will increase.

The time resolution of our measurements was 1 s because the laser irradiation frequency was set at 1 Hz (although the maximum was 110 Hz). Increasing the irradiation frequency and adding the decay curves to smooth them reduces the noise in the phosphorescence signals. However, as shown in Fig. 6, clear decay curves with little noise were obtained by one-shot irradiation, indicating that 200 nJ of pulse energy is sufficient for measurement. Moreover, increasing the pulse irradiation would create excessive singlet oxygen production. Measurement in milliseconds is more than sufficient for a vital reaction. For these reasons, a time resolution of 1 s is sufficient for continuous measurement of oxygen tension.

Reactive oxygen caused by double-wavelength photoexcitation. We monitored RBC velocity and oxygen tension in rat brain microcirculation simultaneously by injecting RBCs labeled with FITC and oxygen probe Pd-TCPP and then exciting these probe dyes by irradiation from a mercury lamp and an Nd:YAG laser, respectively. Exciting photosensitive substances like porphyrin dyes inevitably generates reactive oxygen in microvessels, and reactive oxygen, especially singlet oxygen, causes thrombus formation, which can affect blood flow. We tested continual irradiation of capillaries in intestinum tenue for 10 min but did not observe any change in flow velocity (data not shown). This result depends on not much light energy being needed to measure phosphorescence and the irradiation time being extremely short. In contrast, the excitation light for visualizing the FITC-labeled RBCs came from a mercury lamp and passed through a band-pass filter (450–490 nm) while the shutter was open. The stronger the excitation light, the sharper the images we can create for measuring RBC velocity. When the microvessels were irradiated with high power, however, flow stasis in the vessels was observed within a few minutes. Singlet oxygen must be suppressed to reduce thrombus formation and stasis as much as possible, so we decreased the irradiation power to <5 mW/cm^2 and equipped the recording camera with an image intensifier. We observed no stasis and obtained clear blood flow images.

Phosphorescence emission from tissue under microvessels. When the oxygen tension in a single microvessel in the cerebral cortex is measured, the laser light irradiated through the microscope's objective lens should pass through the microvessel. The measured value may thus be affected by the excitation of Pd-TCPP in the tissue under the targeted microvessel. The oxygen concentration in brain tissue is considerably lower than that of blood in a microvessel, so any mixing of the phosphorescence emitted from intravascular Pd-TCPP with that emitted from interstitial Pd-TCPP would artifactually reduce the measured oxygen concentration in a blood vessel. The effect of this mixing on the measured concentration needs to be investigated. Moreover, the effects of a laser light irradiated not from a confocal system but from a conventional incident-light system also need to be investigated. The main reason that the phosphorescence from the tissue irradiated though a microvessel was extremely weak is attributed to the focusing of the laser light by the objective lens. The irradiation angle of laser light depends on the numerical aperture. The microvessel was irradiated at an angle, not vertically, and the profile of the laser intensity was Gaussian. Consequently, the excitation energy is thought to have been focused in the laser spot area and at the focal depth of the objective lens. For instance, at a wavelength of 532 nm, the focal depth of the objective lens we used, which had a numerical aperture of 0.4, is theoretically 1.7 μm. Therefore, even when scattering by blood is taken into consideration, when the light was focused in a microvessel almost 50 μm in diameter, little excitation light

could have reached the underlying extravascular tissue by passing through the vessel.

In summary, we measured the RBC velocity and oxygen tension in cerebral microcirculation by using the differences in luminescence and wavelength between fluorescence and phosphorescence. With this system, we can acquire information about cerebral microcirculatory distribution and oxygen tension simultaneously and easily. We evaluated our method by examining the factors causing measurement error. Because blood flow and oxygen concentration are associated in organs using large amounts of oxygen, particularly the brain, the heart, and the kidney, simultaneous measurement of the microcirculatory red cell velocity and local oxygen tension should be widely applicable to research.

ACKNOWLEDGMENTS

We thank Mami Ishikawa (Department of Neurosurgery, Keio University School of Medicine, Japan), for assisting with the experiments.

GRANTS

This research was partially supported by a Grant-in-Aid for Young Scientists (B) (15700340, 2003) from the Ministry of Education, Science, Sports and Culture and Kawasaki Medical School Research Project Grant 14-304 and 15-301A.

REFERENCES

1. **Buerk DG, Tsai AG, Intaglietta M, and Johnson PC.** In vivo tissue pO2 measurements in hamster skinfold by recessed pO2 microelectrodes and phosphorescence quenching are in agreement. *Microcirculation* 5: 219–225, 1998.
2. **Erni D, Sakai H, Tsai AG, Banic A, Sigurdsson GH, and Intaglietta M.** Haemodynamics and oxygen tension in the microcirculation of ischaemic skin flaps after neural blockade and haemodilution. *Br J Plast Surg* 52: 565–572, 1999.
3. **Ishikawa M, Sekizuka E, Shimizu K, Yamaguchi N, and Kawase T.** Measurement of RBC velocities in the rat pial arteries with an image-intensified high-speed video camera system. *Microvasc Res* 56: 166–172, 1998.
4. **Ince C and Sinaasappel M.** Microcirculatory oxygenation and shunting in sepsis and shock. *Crit Care Med* 27: 1369–1377, 1999.
5. **Kerger H, Saltzman DJ, Gonzales A, Tsai AG, van Ackern K, Winslow RM, and Intaglietta M.** Microvascular oxygen delivery and interstitial oxygenation during sodium pentobarbital anesthesia. *Anesthesiology* 86: 372–386, 1997.
6. **Kerger H, Torres Filho IP, Rivas M, Winslow RM, and Intaglietta M.** Systemic and subcutaneous microvascular oxygen tension in conscious Syrian golden hamsters. *Am J Physiol Heart Circ Physiol* 268: H802–H810, 1995.
7. **Lahiri S, Rumsey WL, Wilson DF, and Iturriaga R.** Contribution of in vivo microvascular P_{O_2} in the cat carotid body chemotransduction. *J Appl Physiol* 75: 1035–1043, 1993.
8. **Liss AG and Liss P.** Use of a modified oxygen microelectrode and laser-Doppler flowmetry to monitor changes in oxygen tension and microcirculation in a flap. *Plast Reconstr Surg* 105: 2072–2078, 2000.
9. **Parthasarathi K and Lipowsky HH.** Capillary recruitment in response to tissue hypoxia and its dependence on red blood cell deformability. *Am J Physiol Heart Circ Physiol* 277: H2145–H2157, 1999.
10. **Robiolio M, Rumsey WL, and Wilson DF.** Oxygen diffusion and mitochondrial respiration in neuroblastoma cells. *Am J Physiol Cell Physiol* 256: C1207–C1213, 1989.
11. **Rumsey WL, Abbott B, Lo LW, Vinogradov SA, and Wilson DF.** Imaging of oxygen distribution in the surface and deep areas of the kidney. *Adv Exp Med Biol* 411: 591–595, 1997.
12. **Rumsey WL, Vanderkooi JM, and Wilson DF.** Imaging of phosphorescence: a novel method for measuring oxygen distribution in perfused tissue. *Science* 241: 1649–1651, 1988.
13. **Sinaasappel M and Ince C.** Calibration of Pd-porphyrin phosphorescence for oxygen concentration measurements in vivo. *J Appl Physiol* 81: 2297–2303, 1996.
14. **Sinaasappel M, van Iterson M, and Ince C.** Microvascular oxygen pressure in the pig intestine during haemorrhagic shock and resuscitation. *J Physiol* 514: 245–253, 1999.
15. **Shonat RD, Wachman ES, Niu W, Koretsky AP, and Farkas DL.** Near-simultaneous hemoglobin saturation and oxygen tension maps in mouse brain using an AOTF microscope. *Biophys J* 73: 1223–1231, 1997.
16. **Shonat RD, Wilson DF, Riva CE, and Cranstoun SD.** Effect of acute increases in intraocular pressure on intravascular optic nerve head oxygen tension in cats. *Invest Ophthalmol Vis Sci* 33: 3174–3180, 1992.
17. **Song D, Olano M, Wilson DF, Pastuszko A, Tammela O, Nho K, and Shorr RG.** Comparison of the efficacy of blood and PEG-hemoglobin in recovery of newborn piglets from hemorrhagic hypotension. *Transfusion* 35: 552–558, 1995.
18. **Torres Filho IP and Intaglietta M.** Microvessel P_{O_2} measurements by phosphorescence decay method. *Am J Physiol Heart Circ Physiol* 265: H1434–H1438, 1993.
19. **Torres Filho IP, Kerger H, and Intaglietta M.** P_{O_2} measurements in arteriolar networks. *Microvasc Res* 51: 202–212, 1996.
20. **Tsai AG, Friesenecker B, McCarthy M, Sakai H, and Intaglietta M.** Plasma viscosity regulates capillary perfusion during extreme hemodilution in hamster skinfold model. *Am J Physiol Heart Circ Physiol* 275: H2170–H2180, 1998.
21. **Tsukada K, Minamitani H, Sekizuka E, and Oshio C.** Image correlation method for measuring blood flow velocity in microcirculation: correlation 'window' simulation and in vivo image analysis. *Physiol Meas* 21: 459–471, 2000.
22. **Vanderkooi JM and Wilson DF.** A new method for measuring oxygen concentration in biological systems. *Adv Exp Med Biol* 200: 189–193, 1986.
23. **Wilson DF and Cerniglia GJ.** Localization of tumors and evaluation of their state of oxygenation by phosphorescence imaging. *Cancer Res* 52: 3988–3993, 1992.
24. **Wilson DF, Pastuszko A, DiGiacomo JE, Pawlowski M, Schneiderman R, and Delivoria-Papadopoulos M.** Effect of hyperventilation on oxygenation of the brain cortex of newborn piglets. *J Appl Physiol* 70: 2691–2696, 1991.
25. **Wilson DF, Rumsey WL, and Vanderkooi JM.** Oxygen distribution in isolated perfused liver observed by phosphorescence imaging. *Adv Exp Med Biol* 248: 109–15, 1989.
26. **Yonetani M, Huang CC, McGowan J, Lajevardi NS, Pastuszko A, Delivoria-Papadopoulos M, and Wilson DF.** Effect of hemorrhagic hypotension on extracellular level of dopamine, cortical oxygen pressure and blood flow in brain of newborn piglets. *Neurosci Lett* 180: 247–252, 1994.
27. **Zheng L, Golub AS, and Pittman RN.** Determination of P_{O_2} and its heterogeneity in single capillaries. *Am J Physiol Heart Circ Physiol* 271: H365–H372, 1996.

臓器血流と酸素代謝の光・イメージング解析

Photonic imaging analysis of blood flow and oxygen tension in organ microcirculation

南谷晴之(写真)　塚田孝祐

Haruyuki MINAMITANI[1] and Kousuke TSUKADA[2]

慶應義塾大学理工学部物理情報工学科[1]，同医学部医化学教室[2]

◎脳，肝などの実質臓器の微小循環や腫瘍新生血管の血流動態を可視化するとともに，臓器内のミクロレベルでの酸素代謝を同時計測し，組織や細胞の機能変化を解析することはフィジオーム研究の一重要課題となっている．組織や細胞を傷めることなく非接触で計測するには，螢光やリン光を発する分子プローブを細胞に標識し，特定波長の光で励起して螢光イメージやリン光信号を検出する方法が有効である．著者らは多波長励起の光・イメージング解析システムを開発し，FITC 螢光色素で選択的に赤血球を標識し，励起波長 450 nm，螢光波長 520 nm で可視化することで脳虚血に伴う微小循環血流変化を定量解析した．また，酸素感受性色素 Pd ポルフィリンをラット大腿静脈から投与し，波長 532 nm のパルスレーザーで励起し，発光リン光 700 nm をフォトマルで検出して，酸素 quenching 作用によるリン光寿命の変化から微小血管内の酸素分圧を計測することに成功した．

Key word：微小循環，臓器血流，酸素分圧，バイオイメージング，螢光・リン光

臓器微小循環とバイオイメージング

血液は心ポンプの働きで全身に行き渡り，組織に酸素や栄養素を運び，引き換えに二酸化炭素や老廃物を受け取り，組織から排出する役割を担っている．このようなガス交換や物質代謝が行われる領域は，非常に細い細動脈，細静脈，毛細血管，微小リンパ管などの微小循環で構成されており，生命現象の恒常性維持にもっとも重要な役割を果たしている．

近年，増大傾向にある成人病疾患にかかわる脳，腎，肝など各種臓器の微小循環内の血流動態を可視化し，循環機能と疾患との因果関係や薬理効果を詳細に検討する必要性が高まっている．また，循環不全とのかかわりにおいて臓器内のミクロなレベルでの酸素代謝を同時計測し，組織や細胞の機能変化を観測することも重要な課題となっている．一方，ナノテクノロジーは，超微細なレベルで原子・分子を操作したり微小な粒子や機械を作製する技術であるが，バイオ・医療技術と組み合わせたり光・イメージング技術との融合により，生体の分子・オルガネラ・細胞レベルの構造や機能を詳細に解析することを可能としている．

微小循環系の血流や酸素代謝を計測し，定量解析する方法については多くの研究があるが，本稿ではナノプローブとバイオイメージング技術を利用した臓器血流と酸素代謝の光・イメージング解析法を紹介し，虚血脳組織および腫瘍組織の微小循環血流と酸素分圧計測の結果について述べる．

臓器微小循環の光・イメージング解析システム

微小循環研究では対象動物の実質臓器を顕微鏡下に展開し，目標となる細胞・オルガネラなどの形態・動態を可視化することが重要である．その際，フルオロフォア分子，ポルフィリン化合物，螢光蛋白などのナノプローブを生体中に局所投与

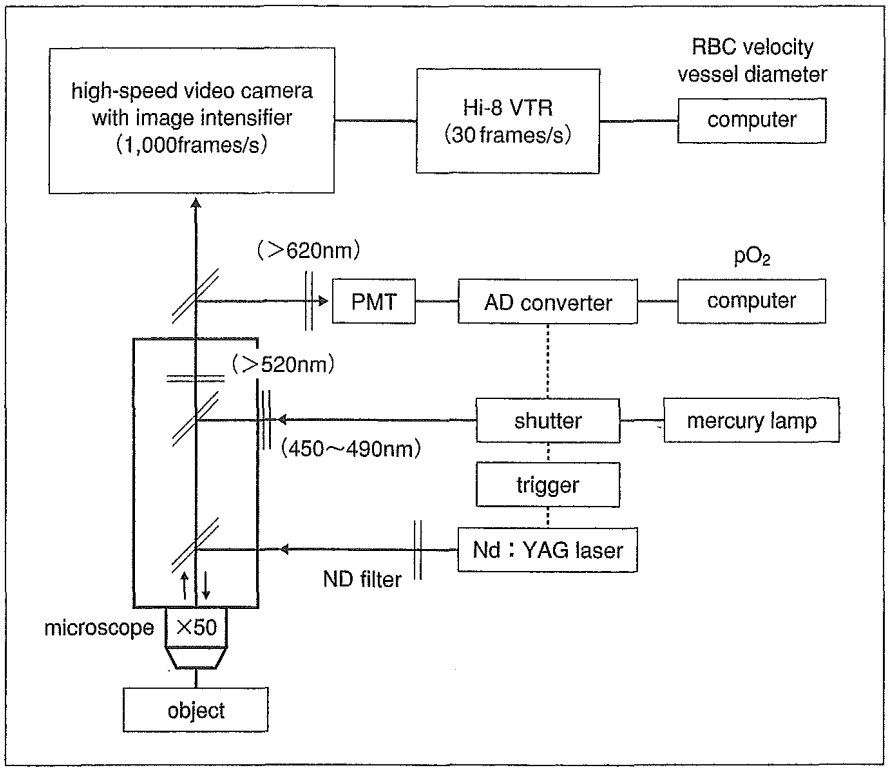

図 1　臓器微小循環の血流と酸素分圧を同時計測する光・イメージング解析システム

し，脳・肝・腎などの臓器微小循環における血流・酸素代謝機能や腫瘍，糖尿病，血栓症などの病態における微小循環障害を分子・細胞レベルでイメージング解析して，障害・再生・治癒機構を解明することが多い．生体分子やオルガネラと結合したナノプローブを使うことにより，超微細な一分子イメージングやイオン種イメージングが可能となるが，超高速度高感度カメラ，高速走査型共焦点レーザー顕微鏡などのイメージングシステムが利用される[1]．

著者らは，顕微鏡下で透過光観測が不可能な厚みを有する臓器において，蛍光プローブを用いた血流可視化と酸素電極を用いることなく，リン光プローブによる血中酸素分圧の同時計測法を開発した[2-4]．血流速度計測システムは，顕微鏡に接続された高速度高感度ビデオカメラ，汎用 Hi8 ビデオレコーダ，画像処理ボードを実装したビデオ制御・画像解析コンピュータ，画像相関法・流速解析ソフトなどで構成される．実質臓器や組織内の微小血管の血行動態は，FITC-dextran(励起波長 488 nm，蛍光波長 520 nm)20 mg/ml を iv 投与し，血漿成分の流動現象を可視化して全血血流動態の定量化を行うことができる．また，あらかじめ循環赤血球の約 5%を採血し，これを体外で蛍光プローブ FITC(励起波長 488 nm，蛍光波長 520 nm)で *ex vivo* 標識した後，返血し，顕微鏡下で微小血管を流れる個々の蛍光標識赤血球の流動現象を可視化することによって赤血球の流速計測が可能となる．白血球の可視化には，アクリジンオレンジ(励起波長 430 nm，蛍光波長 530 nm)0.5 mg/kg を iv 投与し体内染色するか，ローダミン 6G(励起波長 514 nm，蛍光波長 590 nm)50 μg/ml で *ex vivo* 標識して微小血管内の白血球のローリングや粘着数を可視化計測する．血小板の可視化には CFSE(励起波長 494 nm，蛍光波長 520 nm)かローダミン 6G を iv 投与・体内染色するか，CFDASE(励起波長 492 nm，蛍光波長 517 nm)で *ex vivo* 標識して微小血管内の流動，血小板血栓生成動態を可視化評価する．

一方，酸素電極を組織・血管中に刺入することなく非接触・無侵襲に血中酸素分圧を計測するために，リン光発光・酸素プローブ Pd ポルフィリン〔Pd-meso-tetra-(4-carboxyphenyl)-porphyrin：Pd-TCPP〕を用い，光励起後のリン光寿命より酸

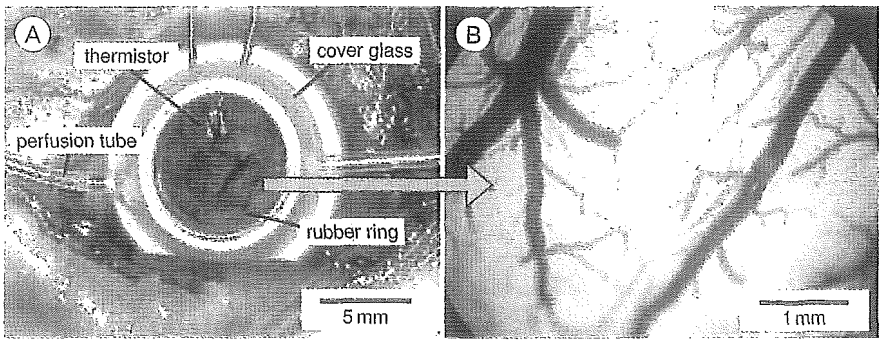

図 2　ラット脳表層の微小循環血流と酸素代謝を観測するための closed cranial window(A)と，微小循環系の血管構築(B)

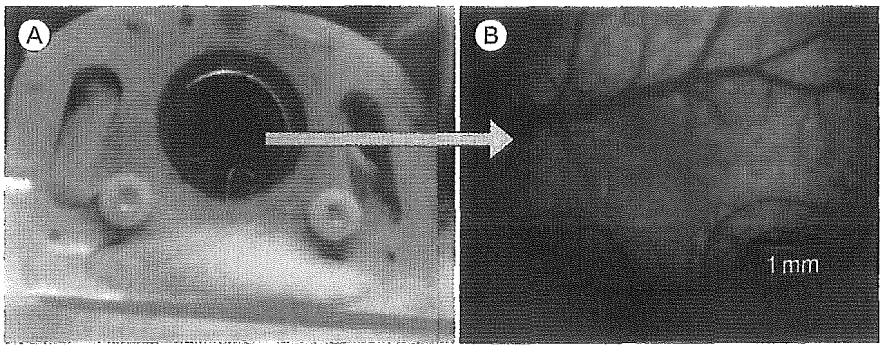

図 3　マウス背部皮膚層の微小循環血流と酸素代謝を観測するための dorsal skinfold chamber(A)と，皮膚層に移植した腫瘍組織と腫瘍新生血管(B)

素分圧を計測する技術を開発した．あらかじめ，対象動物に Pd ポルフィリンを iv 投与し，対象となる微小血管に励起パルス光(Nd：YAG laser SH，波長 532 nm)を照射する．酸素濃度に依存して発光するリン光を 620 nm のロングパスフィルタを介してフォトマルで光電変換し，AD 変換後にパソコンで波形処理してリン光寿命 τ より，つぎの Stern-Volmer 式に基づいて酸素分圧 pO_2 を求める．

$$\tau_0/\tau = 1 + K\tau_0 pO_2$$

ここで τ_0，τ はそれぞれ酸素分圧が 0 および pO_2 mmHg のときのリン光寿命，K は Stern-Volmer 定数であるが，上式からわかるように酸素分圧が高まるとリン光強度は低下，寿命は短縮する．図 1 に示す螢光・リン光ナノプローブを用いたマルチフォトニック・イメージングシステムは著者らによって実用化されており，臓器微小血管内の血流速度・酸素分圧の同時計測だけでなく，異なる波長の光源と受光・受像系を加えることにより，*in vivo* 実験系で多種類の細胞・組織の分子生理機能を解析することができる．

図 2 は，脳表層の微小循環血流と酸素代謝を観測するためのラット頭頂部に設置した closed cranial window と，window 内で観測された細動脈，細静脈，毛細血管などの微小循環系の血管網を示したものである．図 3 はマウス背部皮膚層の微小循環血流と酸素代謝を観測するための dorsal skinfold chamber と，chamber 内で観測された腫瘍組織と腫瘍新生血管網を示したものである．後者は，乳癌細胞 MT060562 を埋め込み増殖させ，それに伴って構築された新生血管である．このような特殊な装置を使い，小動物の対象領域の微小循環血流動態を種々の病態や条件下で慢性的あるいは急性的に観測しイメージング解析することが可能である．

臓臓器血流と酸素代謝の光・イメージング解析

図 4 は closed cranial window 内の Wistar 系雄性ラット脳表層の細動脈と，細静脈を流れる FITC

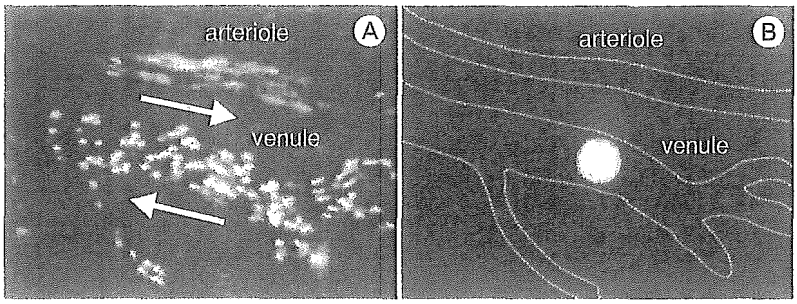

図 4　ラット脳表層の細動脈と細静脈を流れる FITC 標識赤血球(A)と，血中酸素分圧を計測するためのレーザー光スポット(B)

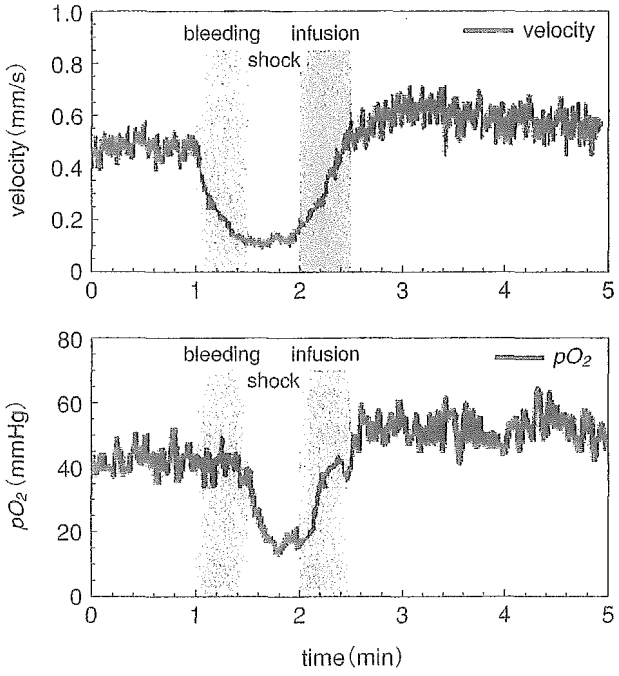

図 5　ラット脳表層細静脈内(図 4)の赤血球流速と血中酸素分圧の時間経過

3 m*l* の脱血ショックと 1 分後の返血再灌流を施行.

図 6　光化学反応による活性酸素産生に基づく脳表層微小血管内の血小板血栓形成

標識赤血球であり，図 4-B の中央の白いスポットは直径約 30 μm の Nd：YAG パルスレーザー(第 2 高調波：532 nm)の照射部位である．この位置を流れる血液中の Pd-TCPP がレーザー励起されてリン光を発するが，放射されるリン光強度と寿命は酸素濃度によって変化する．実験には Pd-TCPP 生食水溶液(10 mg/m*l*)を静脈投与し，事前に求めておいた酸素分圧とリン光寿命の校正曲線に基づき，臓器微小血管内の酸素分圧を計測した．本計測システムでは Nd：YAG レーザー第 2 高調波パルス光の繰返し周波数信号(1 Hz)をトリガーとして電子シャッターを駆動し，FITC 標識赤血球の励起光と Pd-TCPP への励起光を交互に照射し，そのタイミングに合わせて螢光血流収録画像とフォトマルで検出したリン光信号をコンピュータ解析した．

図 5 は観測結果を示したもので，図 4 のラット脳表層細静脈内の赤血球流速と血中酸素分圧の時間経過である．3 m*l* の脱血による急性出血ショックを起こさせたとき，微小循環血流速度および酸素分圧の急激な低下がみられ，1 分後に返血再灌流を施行したところ，双方とも回復するが，前値を上回った後にしだいに前値に収束する傾向が認められた．ラットの肝類洞血管においても急性出血ショックおよび辺血蘇生時の血流動態と酸素分圧を同時計測した結果，臓器特異性があるものの同様な結果が得られ，実質臓器内の虚血，出血性ショックおよび血液再灌流時の微小循環機能の変化を精度よくとらえることができた．

図 6 は光化学反応による活性酸素産生に基づく脳表層微小血管内の血小板血栓形成を示したものであり，脳組織は梗塞により局所的に虚血状態となる．血小板はローダミン 6G を iv 投与して体内

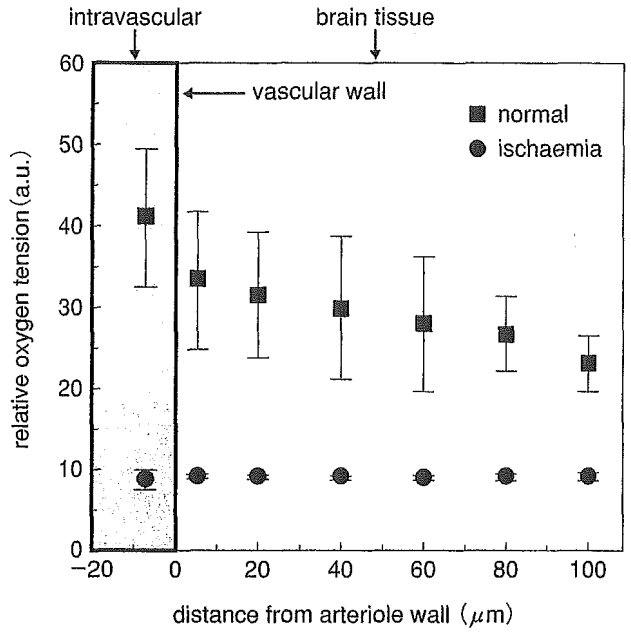

図 7　ラット脳細動脈および周辺脳組織内の血中酸素分圧の空間分布

光化学反応血栓形成法で梗塞した血管と周辺組織では著しい低酸素状態となる．

染色した．このような虚血状態下のラット脳細動脈および周辺組織内の血中酸素分圧の空間分布を示したのが図 7 であり，梗塞した血管と周辺組織では著しい低酸素状態となる．図 7 は相対表示してあるが，梗塞した血管と周辺組織の酸素分圧は 10 mmHg 以下に低下してきわめて重篤な状態に陥る．これに対して正常状態下の血中酸素分圧は高く，組織中の酸素分圧は血管からの距離が隔たるに従って，一定の勾配をもって減少していく様子がわかる．図 3 に示したマウス背部皮膚腫瘍組織内の血流動態と酸素分圧も同様な方法で計測したが，腫瘍新生血管は管径が細く複雑な形態を示し，血管内皮が脆弱で血流速度は低く，酸素分圧もきわめて低い低酸素状態にある．相対的にみて正常な細静脈の酸素分圧は細動脈系の 50％以下であり，また腫瘍新生血管では周辺組織で酸素消費が高いため，正常細静脈系よりさらに低い酸素状態にあることがわかった．

おわりに

血液循環の最大の目的は組織への酸素輸送である．組織とのガス交換を行う微小循環の計測は顕微鏡レベルの観測ゆえに技術的な困難さを伴い，今日まで多くの方法や装置が考案されてきたが，いまだ十分に要求に応えるものがないといっても過言ではない．本稿では，臓器微小循環における血流動態と酸素代謝を非接触・無侵襲で定量的に計測するための光・イメージング解析システムを紹介するとともに，螢光・リン光プローブを用いて赤血球をはじめとする血液細胞の流動と，微小血管内および周辺組織内の酸素分圧を同時計測する方法について述べた．本システムは，脳，肝，腎などの実質臓器微小循環の血流ダイナミクスと，それによる酸素運搬能の定量化に有効であり，糖尿病，高血圧症，高脂血症などの病態における末梢循環障害，それに伴う酸素供給への影響の検討，また病態に対する薬理効果の評価，血液代替物の各種臓器微小循環における酸素運搬能の評価[5]，腫瘍新生血管の特異性評価，種々の病態モデルの生理機能や分子機構の解明などに大きな力を発揮すると考えられる．

文献

1) Minamitani, H. et al.：Imaging and functional analysis of blood flow in organic microcirculation. *J. Pharmacological. Sci.*, **93**(3)：227-233, 2003.
2) Tsukada, K. et al.：Red blood cell velocity and oxygen tension measurement in cerebral microvessels by double-wavelength photoexcitation. *J. Applied Physiol.*, **96**：1561-1568, 2004.
3) Minamitani, H. et al.：Measurement of blood flow and oxygen tension using fluorescent and phosphorescent probes in organ microcirculation. *Microcirculation Annual*, **18**：13-14, 2002.
4) 南谷晴之・他：臓器血流と酸素代謝の光・イメージング解析，公開シンポジウム，ナノとバイオの融合学理構築，産業基盤形成．仙台，2003.
5) Tsukada, K. et al.：Blood flow analysis in cerebral microcirculation during exchange blood transfusion with hemoglobin-encapsulated liposome. *Microcirculation Annual*, **18**：41-42, 2002.

Infusion of the β-adrenergic blocker esmolol attenuates myocardial dysfunction in septic rats*

Takeshi Suzuki, MD; Hiroshi Morisaki, MD; Ryohei Serita, MD; Michiko Yamamoto, BA; Yoshifumi Kotake, MD; Akitoshi Ishizaka, MD; Junzo Takeda, MD

Objective: **Since β-blocker therapy is known to be effective in patients with an injured heart, such as infarction, we designed the present study to examine the protective effects of infusion of the β1-selective blocker esmolol on myocardial function in peritonitis-induced septic rats using an isolated working heart preparation.**

Design: **Randomized animal study.**

Setting: **University research laboratory.**

Subjects: **Thirty-one rats treated with cecal ligation and perforation to evoke peritonitis.**

Interventions: **After cecal ligation and perforation, rats were randomly allocated to the control group (normal saline 2 mL/hr, n = 11), low-dose esmolol group (10 mg/kg/hr, n = 10), or high-dose esmolol group (20 mg/kg/hr, n = 10). After obtaining blood samples for measurement of arterial lactate and tumor necrosis factor-α at 24 hrs, we assessed cardiac output, myocardial oxygen consumption, and cardiac efficiency (cardiac output × peak systolic pressure/myocardial oxygen consumption) at various preloads in an isolated perfused heart preparation.**

Measurements and Main Results: **Esmolol infusion did not cause an elevation of arterial lactate levels but reduced tumor necrosis factor-α concentrations vs. the control group ($p < .05$). Both cardiac output and cardiac efficiency in the esmolol-treated rats were significantly higher throughout the study periods vs. the control group ($p < .05$).**

Conclusions: **Esmolol infusion in sepsis improved oxygen utilization of myocardium and preserved myocardial function. (Crit Care Med 2005; 33:2294–2301)**

Key Words: β1-adrenergic receptor; hyperdynamic sepsis; tumor necrosis factor-α; working heart preparation

Sepsis is a clinical syndrome that arises from an inappropriate and excessive systemic inflammatory response against infection (1). With adequate fluid resuscitation and pharmacologic interventions, systemic hemodynamics of sepsis is characterized by a hyperdynamic circulatory state, resulting in augmentation of oxygen supply to tissues. The importance of sufficient tissue oxygenation was recently addressed in a large-scale clinical trial in which patients at the early stage of sepsis were treated by aggressive management to optimize hemodynamic function (2). During the progression of sepsis, however, regional tissue dysoxia becomes evident and organ dysfunction including heart dysfunction develops (3). Several mechanisms are considered to be responsible for myocardial dysfunction in sepsis (4, 5). For example, proinflammatory cytokines like tumor necrosis factor (TNF)-α have been shown to play a consequential role in the pathogenesis of myocardial dysfunction in sepsis (6, 7). In addition, the number of β-adrenergic receptors was reduced in critically ill patients involving sepsis (8). Few specific strategies, however, have been demonstrated to restore myocardial dysfunction effectively in sepsis.

There is increasing evidence that β-blocker therapy during perioperative periods improves morbidity and mortality in high-risk patients with ischemic heart disease (9). Another study showed a tenfold decrease in the 30-day perioperative incidence of death from cardiac causes and nonfatal myocardial infarction in β-blocker-treated patients undergoing vascular surgery (10). Such protective effects of β-blocker for ischemic myocardium could be accounted for by an improved balance between oxygen supply and consumption (11), regulation of cytokine release (12, 13), and/or restoration of down-regulated β-receptor (14). A question remains, however, whether β-blocker therapy would improve myocardial dysfunction at a hyperdynamic stage of sepsis where cardiac work is augmented. We therefore designed the present study to examine if infusion of esmolol, a β1-selective adrenergic blocker, suppressed the progression of myocardial dysfunction in a normotensive, hyperdynamic model of septic rats.

METHODS

This study protocol was approved by the animal care and use committee of Keio University School of Medicine.

Animal Preparation. Thirty-one male Wistar rats, weighing 320–360 g, were studied after 3- to 7-day acclimatization periods in our laboratory. With sevoflurane anesthesia in oxygen, the jugular vein and carotid artery were cannulated with a catheter (PE50; Intermedic, Sparks, MD) under sterile conditions. Then a laparotomy was performed and a ligature was placed around the cecum immediately distal to the ileocecal valve. The cecum was then punctured twice with an 18-gauge needle. Fol-

*See also p. 2433.

From the Department of Anesthesiology (TS, HM, RS, MY, YK, JT) and Department of Medicine (AI), Keio University School of Medicine, Tokyo, Japan.

Supported by departmental sources.

None of the authors has a commercial association or financial involvement that might pose a conflict of interest in connection with this article.

Address requests for reprints to: Hiroshi Morisaki, MD, Department of Anesthesiology, Keio University School of Medicine, 35 Shinanomachi, Shinjuku-ku, Tokyo 160-8582, Japan. E-mail: anesmrsk@sc.itc.keio.ac.jp.

DOI: 10.1097/01.CCM.0000182796.11329.3B

lowing this preparatory surgery, normal saline was infused at 2 mL/hr via the catheter for the next 24 hrs. Rats were allowed to move freely in cages and have water and laboratory chow *ad libitum*. This preparation was demonstrated to produce normotensive, hyperdynamic sepsis without apparent tissue hypoxia as previously described (15, 16). In addition, to determine *ex vivo* myocardial function of normal rats in our experimental setting, we studied seven sham rats, which received the same catheterization without cecal ligation and perforation (CLP), under the same study protocol described next.

Study Protocol. After the preparatory surgery, the animals were randomized into three groups: Group C (n = 11) received normal saline, group E-10 (n = 10) received esmolol infusion at 10 mg/kg/hr, and group E-20 (n = 10) received esmolol infusion at 20 mg/kg/hr for the next 24 hrs. Our pilot study using a P-U conductance system (ARIA-1, Millar, Houston, TX) demonstrated that esmolol at the rate of 20 mg/kg/hr reduced cardiac output to an approximately 20% lower level compared with the baseline in normal rats under general anesthesia and 10 mg/kg/hr did not significantly influence cardiac output values. At 1 and 24 hrs after randomization, blood samples were taken via the arterial catheter for measurements of white blood cell count, lactate, and proinflammatory cytokines. Twenty-four hours after randomization, animals were reanesthetized with sevoflurane in oxygen. After the intravenous injection of heparin (3000 IU/kg), the hearts of animals were rapidly excised, mounted on a nonrecirculating Langendorff apparatus to allow further preparation, and perfused with modified Krebs-Henseleit solution at 37°C (composition in mM: NaCl 120, KCl 4.8, KH_2PO_4 1.2, $MgSO_4$ 1.2, $CaCl_2$ 1.25, $NaHCO_3$ 25, and glucose 11) as described previously (17). The perfusion buffer was equilibrated with a 95% oxygen/5% CO_2 gas mixture, resulting in a buffer Po_2 >400 mm Hg.

Spontaneous beating heart was used throughout the isolated-perfusion study periods. Following the placement of an aortic cannula, the left atrium was cannulated through the pulmonary vein to allow filling and contraction of the left atrium. With the left atrial cannula open, the Langendorff column was closed and the aortic outflow line opened so that buffer entering through the left atrium could be pumped out of the left ventricle (i.e., the antegrade working mode). Since perfusion of the left atrium provided sufficient heart rate, electrical pacing was obviated to examine left ventricular function in this experiment. During this working mode, a mean aortic pressure of 70 cm H_2O was maintained by a column height equivalent to 70 cm H_2O. Following the ligation of superior and inferior vena cava as well as pulmonary veins to ensure that the coronary effluent passed through the pulmonary artery, the pulmonary artery was cannulated with a 16-gauge steel cannula, and right ventricular outflow was monitored with transit-time ultrasound flowmeter (T206, Transonic Systems, NY) for the measurement of coronary flow. The probe of this flowmeter was also attached to the aortic flow root. Simultaneously, a catheter-tip pressure transducer (postcraniotomy subdural pressure monitoring kit, 110-4G, Neuro Care Group, Camino, CA) was inserted into left ventricle through the left atrium.

After initial 10 mins of perfusion in the working heart model, baseline measurement at 10 cm H_2O preload, by adjusting the height of the left atrial buffer reservoir above the heart, was performed and repeated at various preloads increasing every 2 cm H_2O up to 20 cm H_2O after 15 mins of stabilization.

Specific Measurements and Calculations. Cardiac output (CO) was defined as the sum of coronary and aortic flows in this experimental setting. Left ventricular pressure was continuously monitored with a transducer (postcraniotomy subdural pressure monitoring kit, 110-4G, Neuro Care Group, Camino, CA, and Life Scope II, Nihon Koden, Tokyo) and recorded in a digital recorder (PC208, Sony, Tokyo). Using computer software (Acqknowledge version 3.0 data acquisition systems, Biopac Systems, Goleta, CA, and Microsoft Excel, Microsoft, Redmond, A), left ventricular peak systolic pressure, left ventricular end-diastolic pressure, maximum rate of left ventricular pressure increase (dP/dt_{max}), minimum rate of left ventricular pressure increase (dP/dt_{min}), and heart rate were calculated, based on the averages of five beats. Left ventricular developed pressure, which was regarded as a marker of contractility of the isolated rat heart, was calculated by subtracting left ventricular end-diastolic pressure from left ventricular peak systolic pressure.

The Po_2 of the perfusion medium obtained at preperfusion (inflow) and right ventricular outflow (outflow) was determined by using a standard blood gas analyzer (ABL 700 series, Radiometer Trading, Copenhagen). Oxygen delivery was calculated as inflow oxygen tension, in millimeters of mercury, multiplied by oxygen solubility (24 μL/mL Krebs-Ringer's solution at 760 mm Hg·oxygen and 37°C) and coronary flow (in milliliters per minute). Myocardial oxygen consumption was calculated as oxygen solubility multiplied by the difference between inflow and outflow oxygen tension times coronary flow. Cardiac efficiency was determined as the ratio of cardiac work, the product of cardiac output (mL/min) × left ventricular peak systolic pressure (mm Hg), to myocardial oxygen consumption, as described previously (18).

Biochemical Analyses. The arterial blood samples at 1 and 24 hrs were used to determine white blood cell counts by an analyzer (Celltac, Nihon Kohden, Tokyo, Japan) and lactate by a standard blood gas analyzer (ABL 700 series, Radiometer Trading, Copenhagen). Residual blood was centrifuged at 2500 rpm for 10 mins at 4°C and then stored at −80°C for measurements of cytokines. TNF-α and interleukin-1β were measured in duplicate by enzyme-linked immunosorbent assays using commercially available antibodies (Immunoassay Kit, Biosource International, CA). Briefly, after incubation in the immobilized antibody and a biotinylated antibody specific for each cytokine, streptavidine-peroxidase is added. This binds to the biotinylated antibody to complete the four-member sandwich. Then, a substrate solution is added, which is acted on by the bound enzyme to produce color. The intensity of this colored product is directly proportional to the concentration of each cytokine. The intensity was measured using a plate analyzer (enzyme-linked immunosorbent assay ETY-3A, Toyosokki, Tokyo, Japan).

Immunohistochemical Quantification of Myocardial β1-Receptor. In a separate series of experiments, density of myocardial β1-receptor was determined by immunohistochemistry. In addition to three sham rats, three rats in each group were examined. At 24 hrs after CLP, the rats in three groups were reanesthetized and the hearts were immediately excised and freeze-clamped between blocks of metal cooled in liquid nitrogen and stored at −80°C until the analyses. The β1-adrenergic receptor was analyzed using antihuman β1-adrenergic receptor rabbit polyclonal antibody (PA1-049), which detects β1-adrenergic receptor from mouse and rat tissues. Briefly, sections of hearts were prepared from each of two randomly chosen blocks per tissue per animal and were fixed in dimethyl ketone at 4°C for 20 mins. Then these sections were immersed in 0.3% hydrogen peroxide in methanol for 5 mins to block endogenous peroxidase activity, followed by three rinses in phosphate buffered saline. Sections were incubated with antihuman β1-adrenergic receptor rabbit polyclonal antibody (PA1-049) at a dilution of 1:200 at 4°C overnight. After three rinses in phosphate buffered saline, sections were incubated for 10 mins with secondary antibody: biotin-conjugated mouse and rabbit antigoat immunoglobulin, followed by peroxidase-conjugated streptoavidin. After three rinses in phosphate buffered saline, positive staining was visualized using 3,3'-diaminobenzidine tetrahydrochloride. Slides were then counterstained with hematoxyline. Ten images per each sample were randomly photographed using a microscope attached modular photomicrographic system (Nikon Eclipse TS 100, Nikon, Tokyo). The immunostaining area of the myocardium was measured using a computer software (NIH image 1.63 software, NIH, Bethesda, MD) in a blinded manner, and the ratio of this area to all field of the image was determined as the density of β1-receptors.

Statistical Analysis. Values were described as mean ± SD unless otherwise specified. To compare and contrast the effects of esmolol across the groups during working heart preparation, two-way analysis of variance was employed using the statistical package SPSS/10.0J for Windows (SPSS, Chicago, IL). Where